

Quantum control and Berry phase of electron spins in rotating levitated diamonds in high vacuum

Yuanbin Jin,^{1,*} Kunhong Shen,^{1,*} Peng Ju,¹ Xingyu Gao,¹ Chong Zu,² Alejandro J. Grine,³ and Tongcang Li^{1,4,5,6,†}

¹*Department of Physics and Astronomy, Purdue University, West Lafayette, Indiana 47907, USA*

²*Department of Physics, Washington University, St. Louis, MO, 63130, USA*

³*Sandia National Laboratories, P.O. Box 5800, Albuquerque, NM, 87185, USA*

⁴*Elmore Family School of Electrical and Computer Engineering,
Purdue University, West Lafayette, Indiana 47907, USA*

⁵*Purdue Quantum Science and Engineering Institute,
Purdue University, West Lafayette, Indiana 47907, USA*

⁶*Birck Nanotechnology Center, Purdue University, West Lafayette, Indiana 47907, USA*

(Dated: March 19, 2024)

Levitated diamond particles in high vacuum with internal spin qubits have been proposed for exploring macroscopic quantum mechanics, quantum gravity, and precision measurements. The coupling between spins and particle rotation can be utilized to study quantum geometric phase, create gyroscopes and rotational matter-wave interferometers. However, previous efforts in levitated diamonds struggled with vacuum level or spin state readouts. To address these gaps, we fabricate an integrated surface ion trap with multiple stabilization electrodes. This facilitates on-chip levitation and, for the first time, optically detected magnetic resonance measurements of a nanodiamond levitated in high vacuum. The internal temperature of our levitated nanodiamond remains moderate below 10^{-5} Torr. Impressively, we have driven a nanodiamond to rotate up to 20 MHz (1.2×10^9 rpm), surpassing typical nitrogen-vacancy (NV) center electron spin dephasing rates. Using these NV spins, we observe the effect of the Berry phase arising from particle rotation. In addition, we demonstrate quantum control of spins in a rotating nanodiamond. These results mark an important development in interfacing mechanical rotation with spin qubits, expanding our capacity to study quantum phenomena.

I. INTRODUCTION

Levitated nanoparticles and microparticles in high vacuum [1–3] offer a remarkable degree of isolation from environmental noises, rendering them exceptionally suitable for studying fundamental physics [4–6] and executing precision measurements [7–11]. Recently, the center-of-mass (CoM) motion of levitated nanoparticles in high vacuum has been cooled to the quantum regime [12–14]. Unlike tethered oscillators, levitated particles can also exhibit rotation [15–22], which is intrinsically nonlinear [23, 24]. Beyond rigid-body motion, levitated particles can host embedded spin qubits to provide more functionalities [25, 26]. Notably, levitated nanodiamonds with embedded nitrogen-vacancy (NV) center spin qubits have been proposed for creating massive quantum superpositions [25, 26] to test the limit of quantum mechanics and quantum gravity [27, 28]. The embedded spin qubits can also sense the pseudo-magnetic field [29–31], related to the Barnett effect [32, 33], and the quantum geometric phase [34, 35] associated with particle rotation. The coupling between spin and mechanical rotation can be utilized for building sensitive gyroscopes [36, 37] and rotational matter-wave interferometers [38, 39]. These innovative proposals necessitate levitating diamond particles in a high vacuum, well below 10^{-3} Torr. However, prior

experiments with levitated diamonds struggled with vacuum level or spin state readouts.

Optical levitation of nanodiamonds has been experimentally achieved, but it was restricted to pressures above 1 Torr due to laser-induced heating [40–42]. Earlier studies using Paul traps, or ion traps, have demonstrated spin cooling [43] and angle locking [44] of levitated diamonds. However, they encountered a similar issue: diamond particles were lost when the air pressure was reduced to about 0.01 Torr [43–47]. This phenomenon could be due to the nonideal design of the Paul traps used in those experiments or the heating effects of detection lasers. While nanodiamonds can be levitated in a magneto-gravitational trap [48, 49], reading out the spin state within this setup remains elusive.

In this article, we design and fabricate an integrated surface ion trap (Fig. 1(a)) that incorporates an Ω -shaped stripline to deliver both a low-frequency high voltage for trapping and a microwave for NV spin control. Additionally, it comprises multiple electrodes to stabilize the trap and drive a levitated diamond to rotate. With this advanced Paul trap, we have performed optically detected magnetic resonance (ODMR) measurements of a levitated nanodiamond in high vacuum for the first time. Using NV spins, we measure the internal temperature of the levitated nanodiamond, which remains stable at approximately 350 K under pressures below 10^{-5} Torr. This suggests prospects for levitation in ultra-high vacuum. With a rotating electric field, we have been able to drive a levitated nanodiamond to rotate at high speeds

* These authors contributed equally to this work.

† tcli@purdue.edu

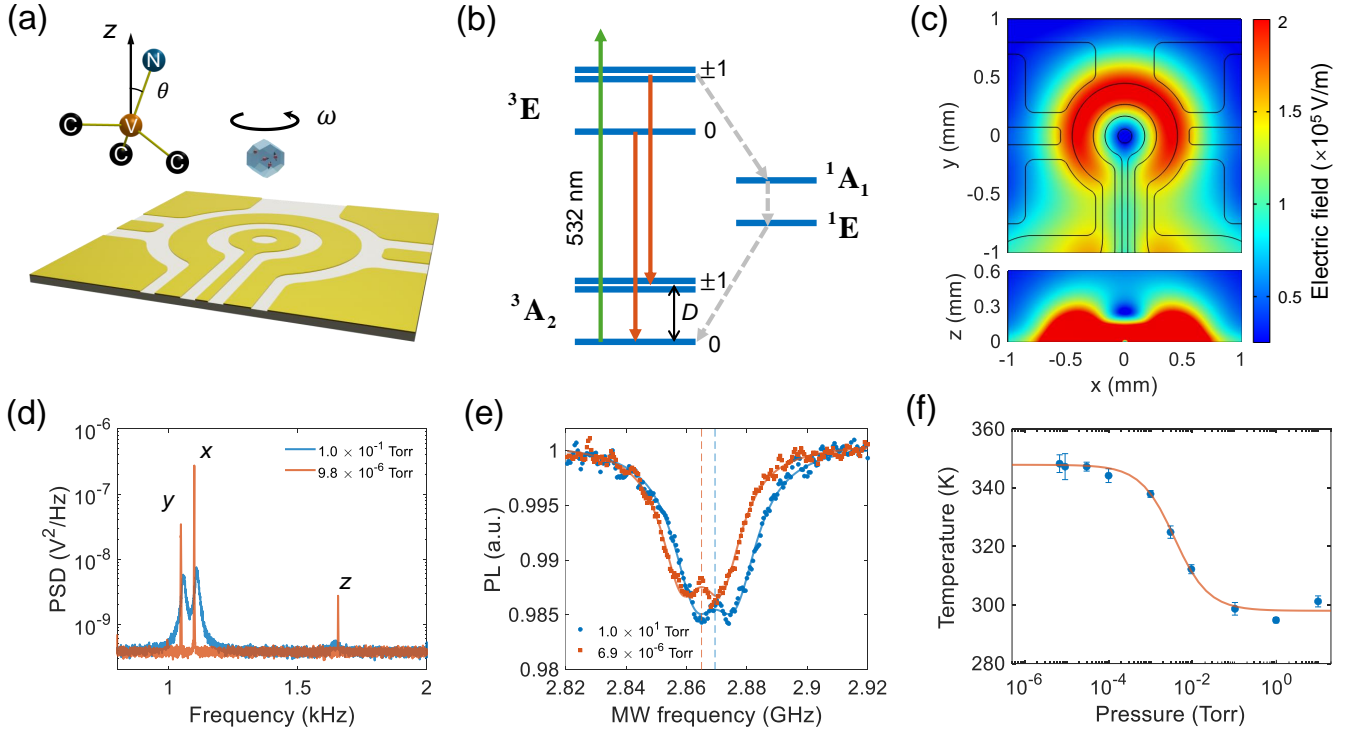


Figure 1. Stable levitation of a nanodiamond in high vacuum. (a) Schematic of a levitated nanodiamond in a surface ion trap. The center ring electrode is grounded (GND). It has a hole at its center for sending a 1064 nm laser to monitor the nanodiamond’s motion. A combination of a low-frequency high voltage (HV) and a high-frequency microwave (MW) is applied to the Ω -shaped circuit to trap the nanodiamond and control the NV centers. (b) Energy level diagram of a diamond NV center. A 532 nm laser (green arrow) excites the NV center. The red solid arrows and gray dashed arrows represent radiative decays and nonradiative decays, respectively. (c) Simulation of the electric field of the ion trap in the xy -plane (top) and in the xz -plane (bottom) when a voltage of 200 V is applied to the Ω -shaped circuit. The trap center is $253 \mu\text{m}$ away from the chip surface. (d) Power spectrum densities (PSDs) of the center-of-mass (CoM) motion of the levitated nanodiamond at the pressure of 0.1 Torr (blue) and 9.8×10^{-6} Torr (red). (e) Optically detected magnetic resonances (ODMRs) of the levitated nanodiamond measured at 10 Torr (blue circles) and 6.9×10^{-6} Torr (red squares). The blue and red dashed lines are the corresponding zero-field splittings. The intensities of the 532 nm laser and the 1064 nm laser are 0.030 W/mm^2 and 0.520 W/mm^2 , respectively. (f) Internal temperature of the levitated nanodiamond as a function of pressure with the same laser intensities as shown in (e).

up to 20 MHz (1.2×10^9 rpm), which is about three orders of magnitudes faster than previous achievements using diamonds mounted on motor spindles [29, 30]. Notably, this rotation speed surpasses the typical dephasing rate of NV spins in the diamond. With embedded NV electron spins in the levitated nanodiamond, we observe the effect of Berry phase generated by the mechanical rotation, which also improves the ODMR spectrum in an external magnetic field. Moreover, we achieve quantum control of NV centers in a rotating levitated nanodiamond. Our work represents a pivotal advancement in interfacing mechanical rotation with spin qubits.

II. RESULTS

A. Levitation of a nanodiamond in high vacuum

In the experiment, we levitate a nanodiamond in vacuum using a surface ion trap (Fig. 1(a)). The surface ion trap is fabricated on a sapphire wafer, which has high transmittance for visible and near-infrared lasers. To achieve levitation of nanodiamonds and quantum control of NV spins simultaneously, we apply both an AC high voltage and a microwave on a Ω -shaped circuit. The AC high voltage has a frequency of about 20 kHz and an amplitude of about 200 V. The microwave has a frequency of a few GHz. They are combined together with a home-made bias tee. The center ring electrode is grounded to generate a trapping center above the chip surface. The four electrodes at the corners are used to compensate the static electric fields from surface charges to minimize the micro-motion of a levitated nanodiamond. Fig. 1(c)

shows a simulated distribution of the electric field of the trap. The trapping center is $253 \mu\text{m}$ away from the chip surface.

The trapping potential depends on the charge to mass ratio (Q/m) of a levitated particle. Thus, it is necessary to increase the charge number of particles for stable levitation in an ion trap. In our experiment, nanodiamonds are charged and sprayed out by electrospray and delivered to the surface ion trap with an extra linear Paul trap. The charge of the sprayed nanodiamond is typically larger than $1000 e$, where e is the elementary charge, enabling a large trapping depth of more than 100 eV (see Supplementary Information for more details). A 532 nm laser is used to excite diamond nitrogen-vacancy (NV) centers and a 1064 nm laser is applied to monitor the nanodiamond's motion. More details of our experimental setup are shown in Supplementary Fig. 1.

A main result of our experiment is that we can levitate a nanodiamond with the surface ion trap in high vacuum, which is a breakthrough as levitated diamond particles were lost around 0.01 Torr in previous studies using ion traps [43–47]. The red curve in Fig. 1(d) shows the power spectrum density (PSD) of the center-of-mass (CoM) motion of a levitated nanodiamond at $9.8 \times 10^{-6} \text{ Torr}$. The radius of the levitated nanodiamond is estimated to be about 264 nm based on its PSDs at 0.01 Torr (Supplementary Fig. 2). Our surface ion trap is remarkably stable in high vacuum. We can levitate a nanodiamond in high vacuum continuously for several weeks.

The internal temperature of a levitated nanodiamond is important as it will affect the spin coherence time and trapping stability. We measure the internal temperature using NV centers. The energy levels of an NV center is shown in Fig. 1(b). We use a 532 nm laser to excite the NV centers and a single photon counting module to detect their photoluminescence. Then we sweep the frequency of a microwave to perform the ODMR measurement of a levitated nanodiamond in the absence of an external magnetic field. Fig. 1(e) shows the ODMRs measured at 10 Torr (blue circles) and $6.9 \times 10^{-6} \text{ Torr}$ (red squares). Based on the fitting of the ODMRs, the corresponding zero-field splittings (blue and red dashed lines) are 2.8694 GHz and 2.8650 GHz , respectively. The internal temperature of the levitated nanodiamond can be obtained from the zero-field splitting (see Methods for details). The measured internal temperature at different pressures are shown in Fig. 1(f). The internal temperature is close to the room temperature at pressures above 0.1 Torr , and increases when we reduce the pressure from 0.1 Torr to 10^{-4} Torr . Finally, it remains stable at approximately 350 K at pressures below $5 \times 10^{-5} \text{ Torr}$. This temperature is low enough to maintain quantum coherence of NV spins for quantum control [50].

The observed phenomena (Fig. 1(f)) arise from the balance between laser-induced heating (Supplementary Fig. 3) and the cooling effects of air molecules and black-body radiation on the internal temperature of a levitated nanodiamond [51, 52]. When the air pressure is high, the

cooling rate due to surrounding air molecules is large and the internal temperature of the levitated nanodiamond is close to the room temperature. However, as air pressure decreases, cooling from air molecules diminishes, leading to a rise in internal temperature. When the pressure is below $5 \times 10^{-5} \text{ Torr}$, the temperature stabilizes as the cooling is dominated by the black body radiation, which is independent of the air pressure.

B. Fast rotation and Berry phase

After a nanodiamond is levitated in high vacuum, we use a rotating electric field to drive the levitated nanodiamond to rotate at high speeds, which also stabilizes the orientation of the levitated nanodiamond. The four electrodes at the corners are applied with AC voltage signals ($A \sin(\omega t + \varphi)$) with the same frequency (ω) and amplitude (A) but different phases (φ) to generate a rotating electric field (Fig. 2(a)). The phases of neighboring signals are different by $\pi/2$. Fig. 2(b) shows the simulation of the electric potential in the xy -plane at $t = 0$. More information can be found in Supplementary Information (Supplementary Fig. 4 and Supplementary Fig. 5). A levitated charged object naturally has an electric dipole moment due to inhomogeneous distribution of charges. In a rotating electric field, the levitated charged particle will rotate due to the torque produced by the interaction between the rotating electric field and the electric dipole of the particle. Fig. 2(c) depicts the PSDs of the rotation at different driving frequencies ($0.1 \text{ MHz} - 20 \text{ MHz}$). The maximum rotation frequency is 20 MHz in the experiment, which is limited by our phase shifters used to generate phase delays between signals on the four electrodes. This is about 3 orders of magnitudes faster than previous achievements using diamonds mounted on electric motor spindles [29, 30]. When the rotation frequency is 100 kHz , the linewidth of the PSD of the rotational signal is fitted to be about $9.9 \times 10^{-5} \text{ Hz}$ (Supplementary Fig. 5(d)), which is limited by the measurement time. This shows that the rotation is extremely stable and is locked to the driving electric signal. With easy control and ultra-stability, this driving scheme enables us to adjust and lock the rotation of the levitated nanodiamond over a large range of frequencies (see Supplementary Information for more details).

The fast rotating diamond with embedded NV spins allows us to observe the effects of the Berry phase due to mechanical rotation. The Berry phase, also known as the geometric phase, is a fundamental aspect of quantum mechanics with applications in multiple fields, including the topological phase of matter and the quantum hall effect [53–57]. The Berry phase in the laboratory frame is equivalent to the pseudo-magnetic field (called the Barnett field in [57]) in the rotating frame: $B_\omega = \omega_r/\gamma$, where γ is the spin gyromagnetic ratio. In this work, the microwave source is fixed in the laboratory frame. Only the levitated diamond is rotating. So, we can observe the

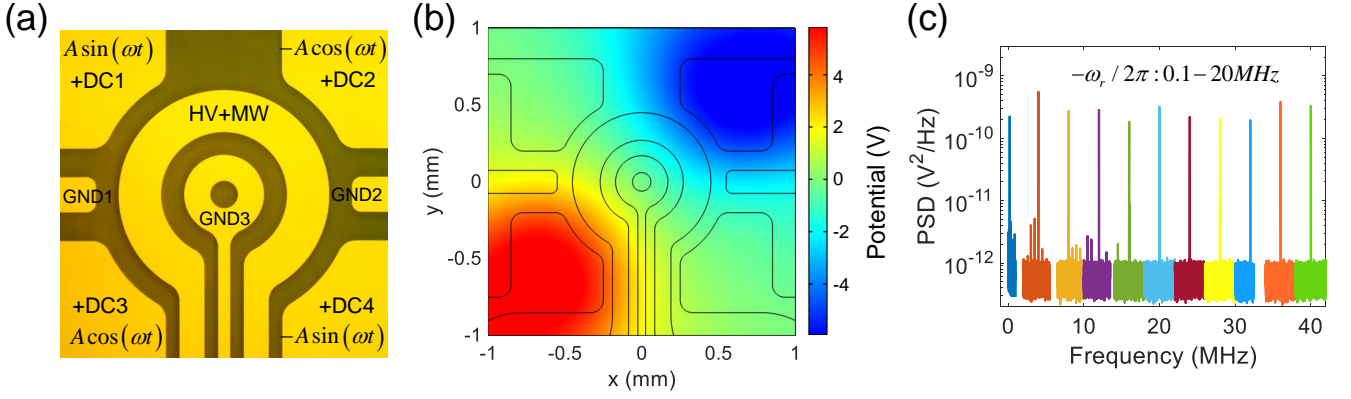


Figure 2. Fast rotation of a levitated nanodiamond. (a) Optical image of the surface ion trap. AC voltage signals ($A \sin(\omega t + \varphi)$) with the same frequency (ω) and amplitude (A) but different phases (φ) are applied to the four corner electrodes to generate a rotating electric field. The phase is different by $\pi/2$ between neighboring electrodes. DC1, DC2, DC3 and DC4 are compensation voltages that minimize the micromotion to stabilize the trap. (b) Simulation of the electric potential in the $z = 253 \mu\text{m}$ plane at $t = 0$. The amplitude is $A = 10 \text{ V}$. (c) PSDs of the rotational motion of the levitated nanodiamond at the rotation frequencies from 0.1 MHz to 20 MHz. The pressure is $1.0 \times 10^{-4} \text{ Torr}$.

effect of the Berry phase due to rotation [57].

In a rotating diamond, the embedded NV centers also follow the rotation with an angular frequency of ω_r (Fig. 3). The levitated nanodiamond in our experiment contains ensembles of NV centers with four groups of orientations. Fig. 3(d) shows a NV center embedded in a nanodiamond rotating around the z axis in the presence

of an external magnetic field. The direction of the magnetic field is along the z axis. The angle between the NV axis and z axis is θ , and the azimuth is $\phi(t)$ relative to the x axis. The Hamiltonian of the rotating NV electron spin in the laboratory frame, neglecting strain effects, can be written as [34]:

$$\begin{aligned}
 H_{lab} &= H_{0,lab} + g\mu_B B S_z = \frac{1}{\hbar} R(t) D S_z^2 R^\dagger(t) + g\mu_B B S_z \\
 &= D\hbar \begin{pmatrix} \cos^2\theta + \frac{\sin^2\theta}{2} + \frac{g\mu_B B}{D} & \frac{e^{-i\phi} \cos\theta \sin\theta}{\sqrt{2}} & \frac{e^{-2i\phi} \sin^2\theta}{2} \\ \frac{e^{i\phi} \cos\theta \sin\theta}{\sqrt{2}} & \sin^2\theta & -\frac{e^{-i\phi} \cos\theta \sin\theta}{\sqrt{2}} \\ \frac{e^{2i\phi} \sin^2\theta}{2} & -\frac{e^{i\phi} \cos\theta \sin\theta}{\sqrt{2}} & \cos^2\theta + \frac{\sin^2\theta}{2} - \frac{g\mu_B B}{D} \end{pmatrix}, \quad (1)
 \end{aligned}$$

where D is the zero-field splitting, $R(t) = R_z(\phi(t)) R_y(\theta)$ is the rotation transformation, and $R_j(\theta) = \exp(-i\theta \mathbf{n} \cdot \mathbf{S})$ for the rotation angle θ around the \mathbf{n} direction, $j = y, z$, and \mathbf{S} is the spin operators. The Stark shift for NV centers induced by the electric field is negligible and hence is not included in the equation. The Hamiltonian possesses three eigenstates $|m_s, t\rangle_{lab}$ ($m_s = 0, \pm 1$). The detailed expressions can be found in the Supplementary Information. Based on its

definition, the Berry phase can be calculated as [57]

$$\gamma_{m_s} = i \int_0^t \langle m_s, t' | \frac{\partial}{\partial t'} | m_s, t' \rangle_{lab} dt' = m_s \omega_r t \cos\theta. \quad (2)$$

Here the Berry phase is calculated for an open-path and is hence gauge-dependent. The spin state of the NV center is observed through the interaction with a microwave magnetic field. In our experiment, the direction of the microwave is in the yz -plane and has a small angle $\theta' = 8.5^\circ$ relative to the z axis, resulting from the asymmetric design of the waveguide. However, the dominant transition probability arises from the longitudinal (z) component. The expected value of the transition probability of the spin states interacting with the microwave can be expressed as

$$\begin{aligned}
 & {}_{lab} \langle \pm 1, t | e^{iH_{lab}t/\hbar} e^{-i\gamma_{\pm 1}} H_{MW,z,lab} e^{i\gamma_0} e^{-iH_{lab}t/\hbar} | 0, t \rangle_{lab} \\
 &= \frac{1}{2} g\mu_B B_{MW} \cos\theta' e^{i(-\omega_{MW} + D \pm g\mu_B B \cos\theta \mp \omega_r \cos\theta)t} {}_{lab} \langle \pm 1, 0 | e^{i\theta S_y} S_z e^{-i\theta S_y} | 0, 0 \rangle_{lab}. \quad (3)
 \end{aligned}$$

According to Eq. 3, the transition of spin states from $|m_s = 0\rangle_{lab}$ to $|m_s = \pm 1\rangle_{lab}$ can be driven by a microwave at the resonance frequency of $D \pm g\mu_B B \cos \theta \mp \omega_r \cos \theta$, where the frequency shift $\mp \omega_r \cos \theta$ is due to the Berry phase induced by the mechanical rotation.

We first investigate the effect of the Berry phase in the absence of an external magnetic field. Fig. 3(a) shows the diagram of a NV center rotating around the z axis without an external magnetic field. To observe the frequency shift due to fast rotation, ODMR measurements of the levitated nanodiamond are carried out at different rotation frequencies. Fig. 3(b) displays ODMRs at rotation frequencies of 0.1 MHz (blue circles) and 14 MHz (red squares). The full width at half maximum (FWHM) of the ODMR at $\omega_r = 2\pi \times 14$ MHz is clearly larger than that at $\omega_r = 2\pi \times 0.1$ MHz, which is caused by the Berry phase due to rotation. The FWHM of the ODMR at different rotation frequencies is shown in Fig. 3(c). The blue circles are the experimental results. The red and orange curves are theoretical results for $\theta = 0^\circ$ and $\theta = 20^\circ$, respectively. Experimentally, the NV ensemble contains NV centers with four orientations. Based on Eq. 3, the broadening of the ODMR spectrum is mainly determined by NV centers with the smallest θ , which have the largest frequency shift induced by the Berry phase (Supplementary Fig. 6). The frequency shift of $\mp \omega_r \cos \theta$ is insensitive to the angle θ for small θ . This explains why the theoretical results for $\theta = 0^\circ$ and $\theta = 20^\circ$ are similar, and both agree well with the experimental results. All data shown in Fig. 3(b),(c) are taken from one levitated diamond.

To determine the frequency shift as a function of the rotational frequency unambiguously, an external magnetic field can be applied to separate the energy levels of NV centers along four different orientations. Here we apply a static magnetic field of about 100 G along the z axis to separate energy levels (Fig. 3(d)). Data shown in Fig. 3(e),(f) are taken from one levitated diamond, which is different from the one used for Fig. 3(b),(c). In Fig. 3(e), the red squares show the ODMR spectrum measured at a rotation frequency of 0.1 MHz. The linewidths of ODMR dips for levitated diamond NV centers are broader than those for fixed NV centers due to the continuous change of NV orientations relative to the magnetic field. Compared with the ODMR spectrum of a levitated nanodiamond without stable rotation (gray circles), the linewidth of each dip for a diamond rotating at 0.1 MHz is narrower. This clearly demonstrates that fast rotation can stabilize the orientation of the levitated nanodiamond. Now we consider the NV centers with the smallest θ (largest Zeeman shift) and the transition between the state $|m_s = 0\rangle$ and the state $|m_s = +1\rangle$ as an example. The electron spin resonance frequency is 3.120 GHz at $\omega_r = 2\pi \times 0.1$ MHz for this transition. The corresponding angle between the NV axis and the rotation axis is $\theta = 20.7^\circ$, which is calculated based on the transition frequency and the magnitude of the external magnetic field. We then measure the resonance

frequency at different clockwise (unless otherwise specified, all are viewed from the positive z direction) rotation frequencies, as shown in Fig. 3(f). The resonance frequency increases following the increase of the rotation frequency. The experimental data points are in between the theoretically calculated curves for $\theta = 20.7^\circ$ (green solid line) and $\theta = 24.0^\circ$ (violet dashed line), indicating the orientation of the NV axes changes slightly when the rotation frequency increases. This is because the electric dipole moment of the levitated nanodiamond is not exactly perpendicular to the axis of the largest or the smallest moment of inertia. Once the rotation frequency increases, the nanodiamond tends to rotate along its stable axis and the driving torque is not large enough to keep its former orientation. The magenta dashed curve is a linear fitting of the resonance frequency. The orientation of the NV center can be calculated by the resonance frequency at the various rotation frequencies. The angle θ changes by approximately 3.3° at $\omega_r = 2\pi \times 10$ MHz, compared with that at $\omega_r = 2\pi \times 0.1$ MHz. A rotating diamond can also serve as a gyroscope [58, 59].

The effect of the Berry phase in a levitated nanodiamond rotating at the counterclockwise direction is shown in Supplementary Fig. 6. The resonance frequency between the state $|m_s = 0\rangle$ and the state $|m_s = +1\rangle$ decreases as the rotation frequency increases for counterclockwise rotation (Supplementary Fig. 6(c)), which is different from that of the levitated nanodiamond rotate clockwise (Fig. 3(f)).

C. Quantum control of fast rotating NV centers

Quantum control of spins is important for creating superposition states [25, 26, 39] and performing advanced quantum sensing protocols [60]. Here we apply a resonant microwave pulse to demonstrate quantum state control of fast rotating NV centers. The spin state can be read out by measuring the emission PL. Because a weak 532 nm laser is used to avoid significant heating, the initialization time should be long enough to prepare the NV spins to the $|m_s = 0\rangle$ state. When the laser intensity is 0.113 W/mm², the initialization time is 1.05 ms (Supplementary Fig. 7). This is shorter than the spin relaxation time ($T_1 \sim 3.6$ ms) of this levitated nanodiamond (Supplementary Fig. 7). We also measure Rabi oscillation of a nanodiamond fixed on a glass cover slip with the same 532 nm laser intensity for comparison. We get similar results for both high and low intensities of the 532 nm laser (Supplementary Fig. 8). Due to the Ω -shape of the microwave antenna, the orientation of the magnetic field of the microwave is located in the yz -plane and slightly different from the z axis with an angle of about $\theta' = 8.5^\circ$ (Fig. 4(a)). So, $\mathbf{n}_{MW} = (-\sin \theta', 0, \cos \theta')$. The effective microwave magnetic field acting on NV spins, with the orientation of $\mathbf{n}_{NV} = (\cos \phi(t) \sin \theta, \sin \phi(t) \sin \theta, \cos \theta)$, changes as a function of the rotation phase $\phi(t)$ of the levitated nanodiamond. The Rabi frequency Ω_{Rabi} can

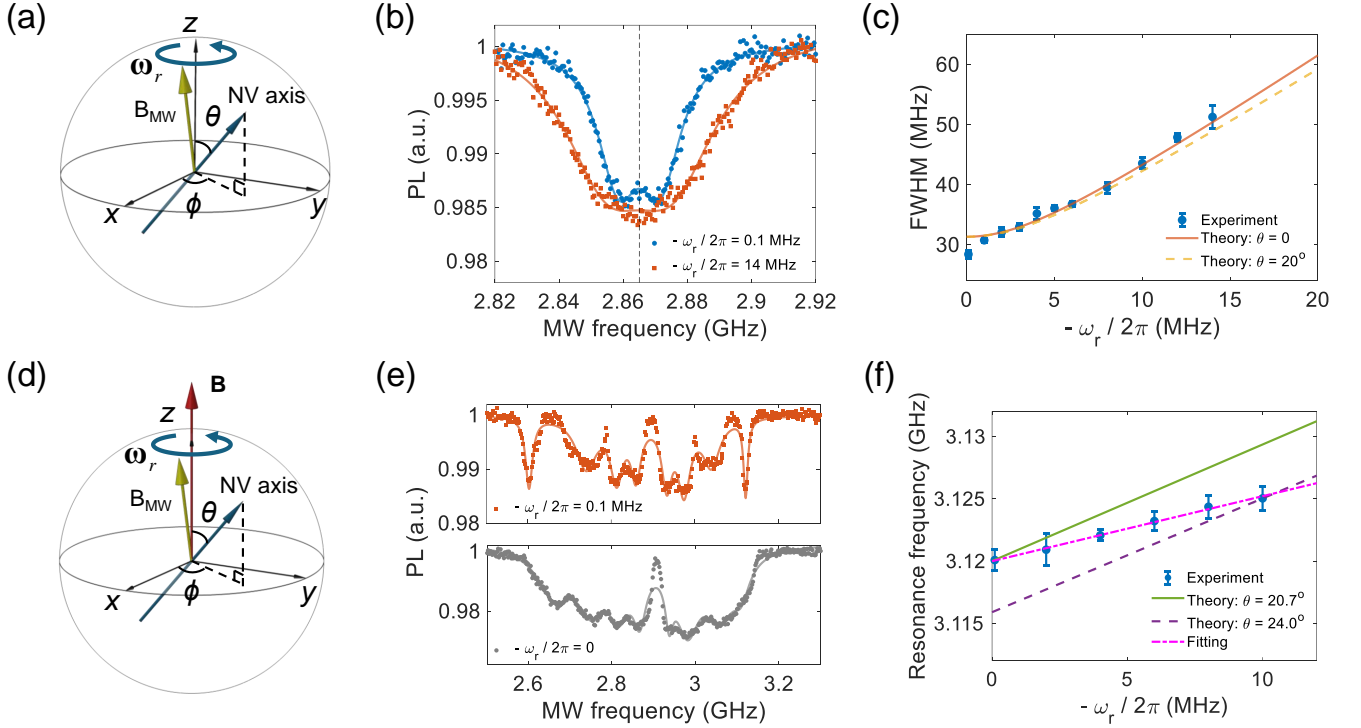


Figure 3. Effects of the Berry phase generated by a rotating nanodiamond. (a) Schematic of an NV center in the nanodiamond rotating around the z axis in the absence of an external magnetic field. The small angle between B_{MW} and the z axis is due to the asymmetric design of the waveguide. (b) ODMRs of the levitated nanodiamond at rotation frequencies of 0.1 MHz (blue circles) and 14 MHz (red squares). (c) Experimentally measured FWHM of the ODMR spectrum as a function of rotation frequency (blue circles). The red solid curve and orange dashed curve are theoretically calculated FWHMs at $\theta = 0^\circ$ and $\theta = 20^\circ$, respectively. (d) Schematic of an NV center in the nanodiamond rotating around the z axis in an external magnetic field. The magnetic field is along the z axis and is about 100 G. (e) The upper panel (red squares) shows the ODMR of the levitated nanodiamond at a rotation frequency of 0.1 MHz and a pressure of 1.0×10^{-4} Torr. The bottom panel (gray circles) shows the ODMR of a nanodiamond without a stable rotation at the pressure of 10 Torr. The corresponding solid curves are the fittings with eight Lorentzian dips. (f) Experimentally measured frequency of the right-most dip of the ODMR spectrum of a NV center as a function of rotation frequency (blue circles). The green solid curve and violet dashed curve are theoretical calculations at $\theta = 20.7^\circ$ and $\theta = 24.0^\circ$, respectively. The magenta dashed curve is a linear fitting of the resonance frequency.

be written as [61, 62]:

$$\Omega_{Rabi} \propto \sqrt{1 - (\cos \theta \cos \theta' - \sin \phi(t) \sin \theta \sin \theta')^2}. \quad (4)$$

Therefore, it is necessary to synchronize the microwave pulse and the rotation phase of the levitated nanodiamond. Fig. 4(b) shows the pulse sequence of the Rabi oscillation measurement. The time gap between the initialization and the readout laser pulses is twice of the rotation period, which allows us to apply the microwave pulse at an arbitrary rotation phase between 0 and 2π .

The measured Rabi oscillations between the state $|m_s = 0\rangle$ and the state $|m_s = +1\rangle$ of NV centers are shown in Fig. 4(d), (e). All these measurements are carried out at a rotation frequency of 100 kHz. The rotation period is 10 μ s which is much longer than the microwave pulse. For NV centers with different orientations, the Rabi frequencies are different. The measured Rabi frequencies are 7.10 MHz, 6.57 MHz and 2.80 MHz when the applied microwave frequencies are 2.936 GHz (dip 1), 3.009 GHz (dip 2) and 3.129 GHz (dip 3), respec-

tively (Fig. 4(d)). Fig. 4(e) shows Rabi oscillations of the NV centers with $\theta = 22^\circ$ at different rotation phases. The blue circles and black squares are measured at the rotation phase of $\phi = \pi/2$ and $\phi = \pi$, respectively. The corresponding Rabi frequencies are 2.72 MHz and 2.23 MHz due to the different projections of the microwave magnetic field along the NV axis. We also apply microwave pulse at other rotation phases to explore how it affects the Rabi frequency. Fig. 4(f) shows the Rabi frequency Ω_{Rabi} for NV centers with $\theta = 22^\circ$ (blue circles) as a function of the rotation phase. The Rabi frequency is smallest at $\phi = 3\pi/2$. The red curve is the theoretical prediction, which agrees well with our experimental results.

D. Feedback cooling of the Center-of-Mass motion

To study quantum spin-mechanics and use a levitated diamond for precision measurements, it will be crucial

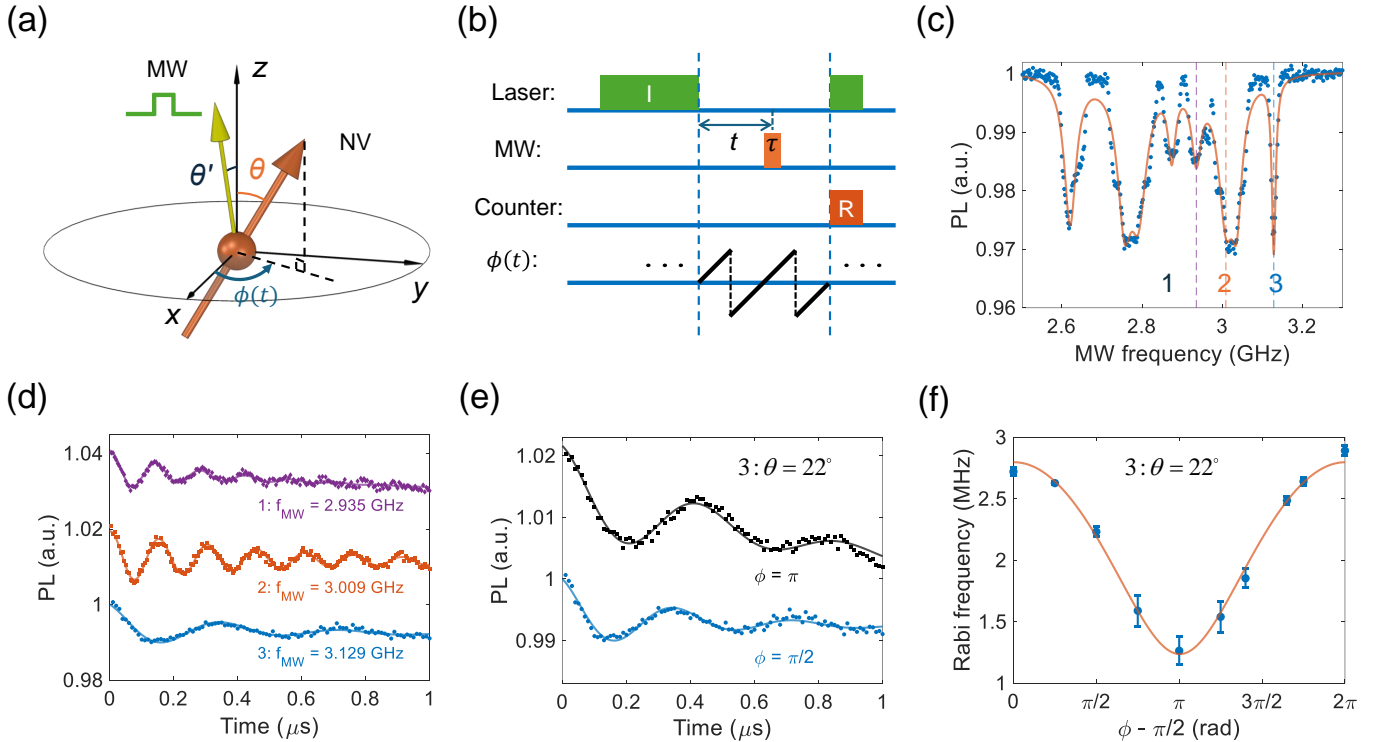


Figure 4. Quantum control of NV centers in a levitated nanodiamond in high vacuum with a rotation frequency of 100 kHz. (a) Schematic of the Rabi oscillation measurement at different rotation phase $\phi(t)$. The angle θ' between the magnetic component of microwave and the z axis is 8.5° . (b) Pulse sequence of the Rabi oscillation measurement. (c) ODMR of the levitated nanodiamond. (d) Measured Rabi oscillations of NV centers at three different orientations. The Rabi frequencies are 7.10 MHz, 6.57 MHz and 2.80 MHz at the ODMR frequencies of 2.935 GHz, 3.009 GHz and 3.129 GHz, respectively. (e) Rabi oscillation of NV centers with $\theta = 22^\circ$ corresponding to the resonance frequency of 3.129 GHz (dip 3). The blue circles and black squares are measured at rotation phase of $\phi = \pi/2$ and $\phi = \pi$, respectively. (f) Rabi frequency at $\theta = 22^\circ$ (blue circles) as a function of the rotation phase ϕ . The red curve is the theoretical prediction.

to reduce the energy of the CoM motion of a levitated diamond. Our integrated Paul trap has multiple electrodes, which can be used for feedback cooling. Because of the high quality factor of the CoM in high vacuum and the low frequency of the CoM motion, we add $\pi/2$ phase delays to the position signals of the levitated diamond to obtain its velocity signals. We then apply electric forces (on the charged diamond) proportional to the velocities but with opposite signs to cool the CoM motion. The schematic diagram is shown in Fig. 5(a). The feedback loop is implemented through an FPGA (Field Programmable Gate Array). The motion signals are read out, followed by band-pass filters, amplifiers and phase delayers, and then fed back to the four electrodes at the corners of the ion trap. Figs. 5(b)-(d) show the PSDs of the CoM motion of a levitated nanodiamond at the pressure of 0.02 Torr without feedback cooling (noFB, blue curves) and at the pressure of 2.0×10^{-5} Torr with feedback cooling (FB, red curves). The orange curves are the corresponding noise floors. Based on the fitting, the final temperature of the CoM motion with feedback cooling are 1.2 ± 0.3 K, 3.5 ± 0.4 K and 86 ± 26 K along the x , y and z directions, respectively. The final temperatures are mainly limited by the small size of the center hole of the

surface ion trap used for forward detection (Figs. 5(a)), which severely limited the NA of the detection system. The cooling efficiency can be improved in the future with backward detection by using the backward scattered light of the levitated diamond collected by the objective lens.

III. DISCUSSION

In conclusion, we have levitated a nanodiamond at pressures below 10^{-5} Torr with a surface ion trap. We performed ODMR measurement of a levitated nanodiamond in high vacuum for the first time. The internal temperature of the levitated nanodiamond remains stable at about 350 K when the pressure is below 5×10^{-5} Torr, which means stable levitation with an ion trap will not be limited by heating even in ultrahigh vacuum. This offers a unique platform for studying fundamental physics, such as massive quantum superposition [25, 26, 39].

Additionally, we apply a rotating electric field that exerts a torque on the levitated nanodiamond to drive it to rotate at high speeds up to 20 MHz. 20 MHz rotation can generate a pseudo-magnetic field of 0.71 mT for an

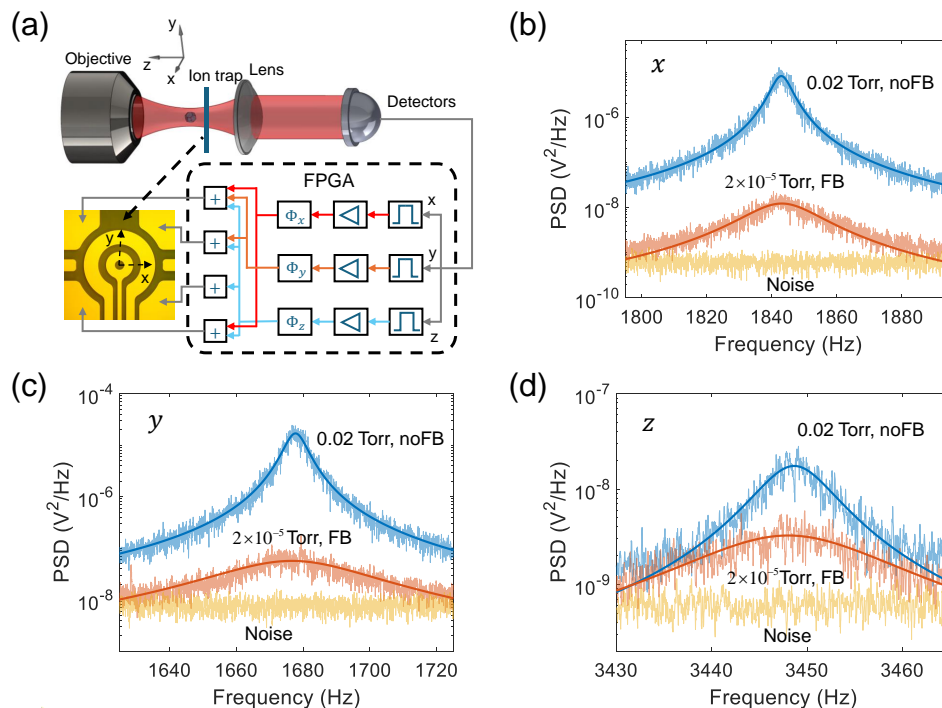


Figure 5. Feedback cooling of the CoM motion of a levitated nanodiamond in the ion trap. (a) Schematic diagram of the feedback cooling method. (b), (c), (d): PSDs of the CoM of the levitated nanodiamond along the (b) x , (c) y and (d) z directions at the pressure of 0.02 Torr without cooling (blue curves) and at the pressure of 2.0×10^{-5} Torr with feedback cooling (red curves). The orange curves are the noise floors. Based on the fitting, the effective temperature of the CoM motion with feedback cooling are 1.2 ± 0.3 K, 3.5 ± 0.4 K and 86 ± 26 K along the x , y and z directions, respectively.

electron spin, and a pseudo-magnetic field of 6.5 T for an ^{14}N nuclear spin. With this method, the rotation frequency of a levitated nanodiamond is extremely stable and easily controllable. The effect of the Berry phase generated by rotation [35] is observed with the embedded NV center electron spins. This will be useful for creating a gyroscope for rotation sensing [36, 58, 59]. We also demonstrate quantum control of rotating NV centers in high vacuum, which will be important for using spins to create nonclassical states of mechanical motion [25, 26, 39]. Using feedback cooling, the CoM of the levitated nanodiamond is cooled in all three directions with a minimum temperature of about 1.2 K along one direction.

The maximum rotation frequency in this experiment is limited by the bandwidth of the multichannel waveform generation system for generating the phase-shifted signals on the four electrodes. The rotation frequency can be much higher with a better waveform generation system. Furthermore, in the presence of a DC external magnetic field, the NV centers within a rotating nanodiamond experience an AC magnetic field. Quantum sensing of an AC magnetic field can have a higher sensitivity compared to that of a DC magnetic field [63]. Consequently, the mechanical rotation can enhance the sensitivity of a magnetometer in measuring DC magnetic fields. By using purer diamond particles, i.e. CVD diamonds, a higher excitation power of the 532 nm laser

can be employed to reduce the initialization time of NV centers.

METHODS

A. Experiment setup and materials

The surface ion trap is fabricated on a sapphire wafer by photolithography. The chip is fixed on a 3D stage and installed in a vacuum chamber. The AC high voltage signal used to levitate nanoparticles and the microwave used for quantum control are combined with a bias tee to be delivered to the chip. A 532 nm laser beam is incident from the bottom to excite diamond NV centers. The photoluminescence (PL) is collected by an objective lens with a numerical aperture (NA) of 0.55. A 1064 nm laser beam focused by the same objective lens is used to monitor both the center-of-mass (CoM) motion and the rotation of the levitated nanoparticle. The PL is separated with the 532 nm laser and the 1064 nm laser by dichroic mirrors. The counting rate and optical spectrum of the PL are measured by a single photon counting module and a spectrometer. The processes of particle launching and trapping are monitored by two cameras.

The diamond particles were acquired from Adamas Nano. The product model is MDNV1umHi10mg (1 mi-

cron Carboxylated Red Fluorescence, 1 mg/mL in DI Water, ~ 3.5 ppm NV). The experimental data shown in the main text of the manuscript are obtained from four different diamond particles. The data presented in Fig. 1, Fig. 2, and Figs. 3(a-c) originate from measurements conducted on the same nanodiamond particle. Figs. 3(d-f) show the data from a second nanodiamond particle, while the data in Fig. 4 is measured using the third nanodiamond particle. Fig. 5 uses the fourth diamond particle.

B. Internal temperature of a levitated nanodiamond

In the experiment, we measure the ODMR of levitated nanodiamond NV centers to detect the internal temperature in the absence of an external magnetic field. The zero-field Hamiltonian of NV center is: $H = DS_z^2/\hbar + E(S_x^2 - S_y^2)/\hbar$, where D is the zero-field energy splitting between the states of $|m_s = 0\rangle$ and $|m_s = \pm 1\rangle$, E is the splitting between the states due to the strain effect. The small splitting between two dips in the ODMR spectra (Fig. 1(e)) without an external magnetic field is due to the E term from strain in the nanodiamond. The zero-field splitting D is dependent on temperature [41, 50]:

$$D = c_0 + c_1 T + c_2 T^2 + c_3 T^3 + \Delta_{pressure} + \Delta_{strain}, \quad (5)$$

where $c_0 = 2.8697$ GHz, $c_1 = 9.7 \times 10^{-5}$ GHz/K, $c_2 = -3.7 \times 10^{-7}$ GHz/K², $c_3 = 1.7 \times 10^{-10}$ GHz/K³, $\Delta_{pressure} = 1.5 \times 10^{-6}$ GHz/bar, and Δ_{strain} is caused by the internal strain effect. $\Delta_{pressure}$ is smaller and can be neglected in vacuum. Fig. 1(e) is the ODMR measured at the pressure of 10 Torr (blue circles) and 6.9×10^{-6} Torr (red squares). The zero-field splitting obtained by fitting can be used to calculate the temperature of the levitated nanodiamond.

The internal temperature T of a levitated nanodiamond is determined by the balance between heating and cooling effects [51, 52]:

$$A_a = A_{gas} p (T - T_0) + A_{bb} (T^5 - T_0^5), \quad (6)$$

where $A_a = \sum_{\lambda} \eta_{\lambda} I_{\lambda} V$ is the heating of the excitation laser ($\lambda = 532$ nm) and the detecting laser ($\lambda = 1064$ nm), η_{λ} is the absorption coefficient of nanodiamond and I_{λ} is the laser intensity, V is the volume of nanodiamond. The first term at the right side of the equation is the cooling rate caused by gas molecule collisions, $A_{gas} = \frac{1}{2} \kappa \pi R^2 v T_0 \frac{\gamma' + 1}{\gamma' - 1}$, $\kappa \approx 1$ is the thermal accommodation coefficient, R is the radius of nanodiamond, v is the mean thermal speed of gas molecules, γ' is the specific heat ratio ($\gamma' = 7/5$ for air near room temperature), p is the pressure, T_0 is the thermal temperature. The last term is the cooling rate of black-body radiation. $A_{bb} = 72 \zeta(5) V k_B^5 / (\pi^2 c^3 \hbar^4) \text{Im} \left(\frac{\varepsilon - 1}{\varepsilon + 2} \right)$, where $\zeta(5) \approx 1.04$ is the Riemann zeta function, k_B is the Boltzmann constant, c is the vacuum light speed, \hbar is the reduced Planck's constant, ε is a constant and time-independent permittivity of nanodiamond across the black-body radiation spectrum. By measuring the internal temperature as a function of the intensities of the 532 nm laser and the 1064 nm laser, the absorption coefficients of the nanodiamond are estimated to be 111 cm^{-1} at 532 nm and 5.87 cm^{-1} at 1064 nm (Supplementary Fig. 3).

ACKNOWLEDGMENTS

We thank Jun Ye for helpful discussions. We acknowledge the support from the National Science Foundation under Grant PHY-2110591 and the Office of Naval Research under Grant No. N00014-18-1-2371. This project is also partially supported by the Laboratory Directed Research and Development program at Sandia National Laboratories, a multimission laboratory managed and operated by National Technology and Engineering Solutions of Sandia LLC, a wholly owned subsidiary of Honeywell International Inc., for the U.S. Department of Energy's National Nuclear Security Administration under Contract No. DE-NA0003525. This paper describes objective technical results and analysis. Any subjective views or opinions that might be expressed in the paper do not necessarily represent the views of the U.S. Department of Energy or the United States Government.

-
- [1] C. Gonzalez-Ballester, M. Aspelmeyer, L. Novotny, R. Quidant, and O. Romero-Isart, Levitodynamics: Levitation and control of microscopic objects in vacuum, *Science* **374**, eabg3027 (2021).
 - [2] J. Millen, T. S. Monteiro, R. Pettit, and A. N. Vamivakas, Optomechanics with levitated particles, *Reports on Progress in Physics* **83**, 026401 (2020).
 - [3] G. Winstone, M. Bhattacharya, A. A. Geraci, T. Li, P. J. Pauzauskie, and N. Vamivakas, Levitated optomechanics: A tutorial and perspective, arXiv preprint arXiv:2307.11858 (2023).
 - [4] O. Romero-Isart, A. C. Pflanzer, F. Blaser, R. Kaltenbaek, N. Kiesel, M. Aspelmeyer, and J. I. Cirac, Large quantum superpositions and interference of massive nanometer-sized objects, *Phys. Rev. Lett.* **107**, 020405 (2011).
 - [5] G. Afek, D. Carney, and D. C. Moore, Coherent scattering of low mass dark matter from optically trapped sensors, *Phys. Rev. Lett.* **128**, 101301 (2022).
 - [6] P. Yin, R. Li, C. Yin, X. Xu, X. Bian, H. Xie, C.-K. Duan, P. Huang, J.-h. He, and J. Du, Experiments with levitated force sensor challenge theories of dark energy,

- Nature Physics* **18**, 1181 (2022).
- [7] A. A. Geraci, S. B. Papp, and J. Kitching, Short-range force detection using optically cooled levitated microspheres, *Phys. Rev. Lett.* **105**, 101101 (2010).
- [8] E. Hebestreit, M. Frimmer, R. Reimann, and L. Novotny, Sensing static forces with free-falling nanoparticles, *Phys. Rev. Lett.* **121**, 063602 (2018).
- [9] T. M. Hoang, Y. Ma, J. Ahn, J. Bang, F. Robicheaux, Z.-Q. Yin, and T. Li, Torsional optomechanics of a levitated nonspherical nanoparticle, *Phys. Rev. Lett.* **117**, 123604 (2016).
- [10] Y. Zheng, L.-M. Zhou, Y. Dong, C.-W. Qiu, X.-D. Chen, G.-C. Guo, and F.-W. Sun, Robust optical-levitation-based metrology of nanoparticle's position and mass, *Physical review letters* **124**, 223603 (2020).
- [11] S. Zhu, Z. Fu, X. Gao, C. Li, Z. Chen, Y. Wang, X. Chen, and H. Hu, Nanoscale electric field sensing using a levitated nano-resonator with net charge, *Photonics Research* **11**, 279 (2023).
- [12] U. Delić, M. Reisenbauer, K. Dare, D. Grass, V. Vuletić, N. Kiesel, and M. Aspelmeyer, Cooling of a levitated nanoparticle to the motional quantum ground state, *Science* **367**, 892 (2020).
- [13] L. Magrini, P. Rosenzweig, C. Bach, A. Deutschmann-Olek, S. G. Hofer, S. Hong, N. Kiesel, A. Kugi, and M. Aspelmeyer, Real-time optimal quantum control of mechanical motion at room temperature, *Nature* **595**, 373 (2021).
- [14] F. Tebbenjohanns, M. L. Mattana, M. Rossi, M. Frimmer, and L. Novotny, Quantum control of a nanoparticle optically levitated in cryogenic free space, *Nature* **595**, 378 (2021).
- [15] Y. Arita, M. Mazilu, and K. Dholakia, Laser-induced rotation and cooling of a trapped microgyroscope in vacuum, *Nature Communications* **4**, 2374 (2013).
- [16] S. Kuhn, B. A. Stickler, A. Kosloff, F. Patolsky, K. Hornberger, M. Arndt, and J. Millen, Optically driven ultra-stable nanomechanical rotor, *Nature Communications* **8**, 1670 (2017).
- [17] R. Reimann, M. Doderer, E. Hebestreit, R. Diehl, M. Frimmer, D. Windey, F. Tebbenjohanns, and L. Novotny, GHz rotation of an optically trapped nanoparticle in vacuum, *Phys. Rev. Lett.* **121**, 033602 (2018).
- [18] J. Ahn, Z. Xu, J. Bang, Y.-H. Deng, T. M. Hoang, Q. Han, R.-M. Ma, and T. Li, Optically levitated nanodumbbell torsion balance and GHz nanomechanical rotor, *Phys. Rev. Lett.* **121**, 033603 (2018).
- [19] J. Ahn, Z. Xu, J. Bang, P. Ju, X. Gao, and T. Li, Ultrasensitive torque detection with an optically levitated nanorotor, *Nature Nanotechnology* **15**, 89 (2020).
- [20] Y. Jin, J. Yan, S. J. Rahman, J. Li, X. Yu, and J. Zhang, 6 GHz hyperfast rotation of an optically levitated nanoparticle in vacuum, *Photon. Res.* **9**, 1344 (2021).
- [21] K. Zeng, X. Xu, Y. Wu, X. Wu, and D. Xiao, Optically levitated gyroscopes with a mhz rotating micro-rotor, arXiv preprint arXiv:2308.09085 (2023).
- [22] P. Ju, Y. Jin, K. Shen, Y. Duan, Z. Xu, X. Gao, X. Ni, and T. Li, Near-field ghz rotation and sensing with an optically levitated nanodumbbell, arXiv preprint arXiv:2301.10868 (2023).
- [23] Y. Ma, K. E. Khosla, B. A. Stickler, and M. Kim, Quantum persistent tennis racket dynamics of nanorotors, *Physical Review Letters* **125**, 053604 (2020).
- [24] B. A. Stickler, K. Hornberger, and M. Kim, Quantum rotations of nanoparticles, *Nature Reviews Physics* **3**, 589 (2021).
- [25] Z.-q. Yin, T. Li, X. Zhang, and L. M. Duan, Large quantum superpositions of a levitated nanodiamond through spin-optomechanical coupling, *Phys. Rev. A* **88**, 033614 (2013).
- [26] M. Scala, M. S. Kim, G. W. Morley, P. F. Barker, and S. Bose, Matter-wave interferometry of a levitated thermal nano-oscillator induced and probed by a spin, *Phys. Rev. Lett.* **111**, 180403 (2013).
- [27] S. Bose, A. Mazumdar, G. W. Morley, H. Ulbricht, M. Toroš, M. Paternostro, A. A. Geraci, P. F. Barker, M. Kim, and G. Milburn, Spin entanglement witness for quantum gravity, *Physical review letters* **119**, 240401 (2017).
- [28] C. Marletto and V. Vedral, Gravitationally induced entanglement between two massive particles is sufficient evidence of quantum effects in gravity, *Physical review letters* **119**, 240402 (2017).
- [29] A. Wood, E. Lilette, Y. Y. Fein, V. S. Perunicic, L. Hollenberg, R. E. Scholten, and A. M. Martin, Magnetic pseudo-fields in a rotating electron–nuclear spin system, *Nature Physics* **13**, 1070 (2017).
- [30] A. A. Wood, E. Lilette, Y. Y. Fein, N. Tomek, L. P. McGuinness, L. C. L. Hollenberg, R. E. Scholten, and A. M. Martin, Quantum measurement of a rapidly rotating spin qubit in diamond, *Science Advances* **4**, eaar7691 (2018).
- [31] H. Chudo, M. Ono, K. Harii, M. Matsuo, J. Ieda, R. Haruki, S. Okayasu, S. Maekawa, H. Yasuoka, and E. Saitoh, Observation of barnett fields in solids by nuclear magnetic resonance, *Applied Physics Express* **7**, 063004 (2014).
- [32] S. J. Barnett, Magnetization by rotation, *Phys. Rev.* **6**, 239 (1915).
- [33] S. J. Barnett, Gyromagnetic and electron-inertia effects, *Rev. Mod. Phys.* **7**, 129 (1935).
- [34] D. Maclaurin, M. W. Doherty, L. C. L. Hollenberg, and A. M. Martin, Measurable quantum geometric phase from a rotating single spin, *Phys. Rev. Lett.* **108**, 240403 (2012).
- [35] X.-Y. Chen, T. Li, and Z.-Q. Yin, Nonadiabatic dynamics and geometric phase of an ultrafast rotating electron spin, *Science Bulletin* **64**, 380 (2019).
- [36] M. P. Ledbetter, K. Jensen, R. Fischer, A. Jarmola, and D. Budker, Gyroscopes based on nitrogen-vacancy centers in diamond, *Phys. Rev. A* **86**, 052116 (2012).
- [37] H. Zhang and Z.-Q. Yin, Highly sensitive gyroscope based on a levitated nanodiamond, *Optics Express* **31**, 8139 (2023).
- [38] Y. Ma, T. M. Hoang, M. Gong, T. Li, and Z.-q. Yin, Proposal for quantum many-body simulation and torsional matter-wave interferometry with a levitated nanodiamond, *Physical Review A* **96**, 023827 (2017).
- [39] C. C. Rusconi, M. Perdriat, G. Hétet, O. Romero-Isart, and B. A. Stickler, Spin-controlled quantum interference of levitated nanorotors, *Phys. Rev. Lett.* **129**, 093605 (2022).
- [40] L. P. Neukirch, E. Von Haartman, J. M. Rosenholm, and A. Nick Vamivakas, Multi-dimensional single-spin nano-optomechanics with a levitated nanodiamond, *Nature Photonics* **9**, 653 (2015).

- [41] T. M. Hoang, J. Ahn, J. Bang, and T. Li, Electron spin control of optically levitated nanodiamonds in vacuum, *Nature Communications* **7**, 12250 (2016).
- [42] A. C. Frangeskou, A. T. M. A. Rahman, L. Gines, S. Mandal, O. A. Williams, P. F. Barker, and G. W. Morley, Pure nanodiamonds for levitated optomechanics in vacuum, *New Journal of Physics* **20**, 043016 (2018).
- [43] T. Delord, P. Huillery, L. Nicolas, and G. Hétet, Spin-cooling of the motion of a trapped diamond, *Nature* **580**, 56 (2020).
- [44] M. Perdriat, P. Huillery, C. Pellet-Mary, and G. Hétet, Angle locking of a levitating diamond using spin diamagnetism, *Physical Review Letters* **128**, 117203 (2022).
- [45] T. Delord, L. Nicolas, M. Bodini, and G. Hétet, Diamonds levitating in a Paul trap under vacuum: Measurements of laser-induced heating via nv center thermometry, *Applied Physics Letters* **111** (2017).
- [46] G. P. Conangla, A. W. Schell, R. A. Rica, and R. Quidant, Motion control and optical interrogation of a levitating single nitrogen vacancy in vacuum, *Nano letters* **18**, 3956 (2018).
- [47] M. Perdriat, C. C. Rusconi, T. Delord, P. Huillery, C. Pellet-Mary, B. A. Stickler, and G. Hétet, Spin readout of the motion of levitated electrically rotated diamonds, arXiv preprint arXiv:2309.01545 (2023).
- [48] J.-F. Hsu, P. Ji, C. W. Lewandowski, and B. D'Urso, Cooling the motion of diamond nanocrystals in a magneto-gravitational trap in high vacuum, *Scientific reports* **6**, 30125 (2016).
- [49] M. C. O'Brien, S. Dunn, J. E. Downes, and J. Twamley, Magneto-mechanical trapping of micro-diamonds at low pressures, *Applied Physics Letters* **114**, 053103 (2019).
- [50] D. M. Toyli, D. J. Christle, A. Alkauskas, B. B. Buckley, C. G. Van de Walle, and D. D. Awschalom, Measurement and control of single nitrogen-vacancy center spins above 600 K, *Phys. Rev. X* **2**, 031001 (2012).
- [51] F. Liu, K. Daun, D. Snelling, and G. Smallwood, Heat conduction from a spherical nano-particle: status of modeling heat conduction in laser-induced incandescence, *Applied Physics B* **83**, 355 (2006).
- [52] D. E. Chang, C. A. Regal, S. B. Papp, D. J. Wilson, J. Ye, O. Painter, H. J. Kimble, and P. Zoller, Cavity opto-mechanics using an optically levitated nanosphere, *Proceedings of the National Academy of Sciences* **107**, 1005 (2010).
- [53] R. Tycko, Adiabatic rotational splittings and berry's phase in nuclear quadrupole resonance, *Phys. Rev. Lett.* **58**, 2281 (1987).
- [54] Y. Zhang, Y.-W. Tan, H. L. Stormer, and P. Kim, Experimental observation of the quantum hall effect and berry's phase in graphene, *Nature* **438**, 201 (2005).
- [55] P. J. Leek, J. M. Fink, A. Blais, R. Bianchetti, M. Göppl, J. M. Gambetta, D. I. Schuster, L. Frunzio, R. J. Schoelkopf, and A. Wallraff, Observation of berry's phase in a solid-state qubit, *Science* **318**, 1889 (2007).
- [56] D. Xiao, M.-C. Chang, and Q. Niu, Berry phase effects on electronic properties, *Rev. Mod. Phys.* **82**, 1959 (2010).
- [57] H. Chudo, M. Matsuo, S. Maekawa, and E. Saitoh, Barnett field, rotational doppler effect, and berry phase studied by nuclear quadrupole resonance with rotation, *Phys. Rev. B* **103**, 174308 (2021).
- [58] V. V. Soshenko, S. V. Bolshedvorskii, O. Rubinas, V. N. Sorokin, A. N. Smolyaninov, V. V. Vorobyov, and A. V. Akimov, Nuclear spin gyroscope based on the nitrogen vacancy center in diamond, *Phys. Rev. Lett.* **126**, 197702 (2021).
- [59] A. Jarmola, S. Lourette, V. M. Acosta, A. G. Birdwell, P. Blümler, D. Budker, T. Ivanov, and V. S. Malinovsky, Demonstration of diamond nuclear spin gyroscope, *Science Advances* **7**, eabl3840 (2021).
- [60] C. L. Degen, F. Reinhard, and P. Cappellaro, Quantum sensing, *Rev. Mod. Phys.* **89**, 035002 (2017).
- [61] A. A. Wood, L. C. L. Hollenberg, R. E. Scholten, and A. M. Martin, Observation of a quantum phase from classical rotation of a single spin, *Phys. Rev. Lett.* **124**, 020401 (2020).
- [62] A. A. Wood, R. M. Goldblatt, R. E. Scholten, and A. M. Martin, Quantum control of nuclear-spin qubits in a rapidly rotating diamond, *Phys. Rev. Res.* **3**, 043174 (2021).
- [63] A. A. Wood, A. Stacey, and A. M. Martin, dc quantum magnetometry below the ramsey limit, *Phys. Rev. Appl.* **18**, 054019 (2022).
- [64] T. H. Kim, P. F. Herskind, T. Kim, J. Kim, and I. L. Chuang, Surface-electrode point paul trap, *Phys. Rev. A* **82**, 043412 (2010).
- [65] H.-K. Li, E. Urban, C. Noel, A. Chuang, Y. Xia, A. Ransford, B. Hemmerling, Y. Wang, T. Li, H. Häffner, and X. Zhang, Realization of translational symmetry in trapped cold ion rings, *Phys. Rev. Lett.* **118**, 053001 (2017).
- [66] J. Fremerey, Spinning rotor vacuum gauges, *Vacuum* **32**, 685 (1982).
- [67] J. R. Maze, P. L. Stanwix, J. S. Hodges, S. Hong, J. M. Taylor, P. Cappellaro, L. Jiang, M. V. G. Dutt, E. Togan, A. S. Zibrov, A. Yacoby, R. L. Walsworth, and M. D. Lukin, Nanoscale magnetic sensing with an individual electronic spin in diamond, *Nature* **455**, 644 (2008).

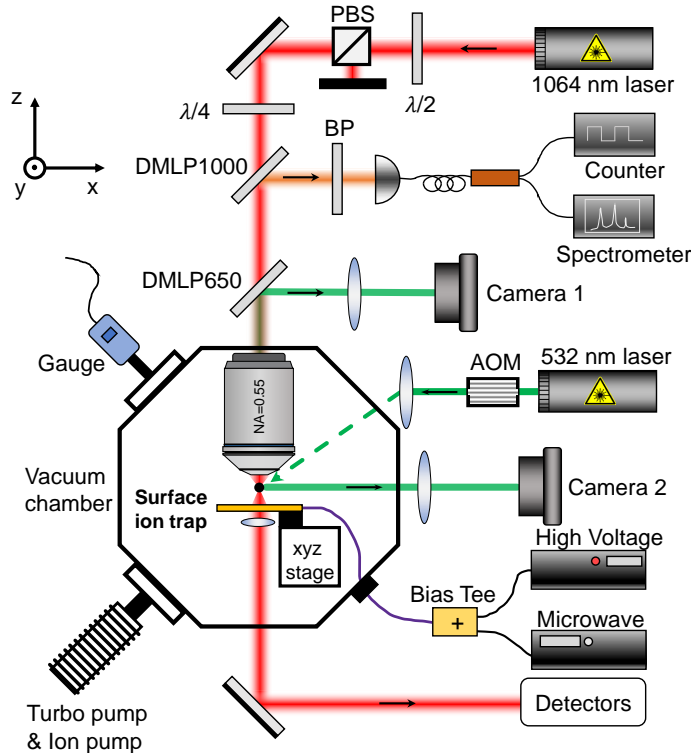
SUPPLEMENTARY INFORMATION

Appendix A: Experiment setup and surface ion trap

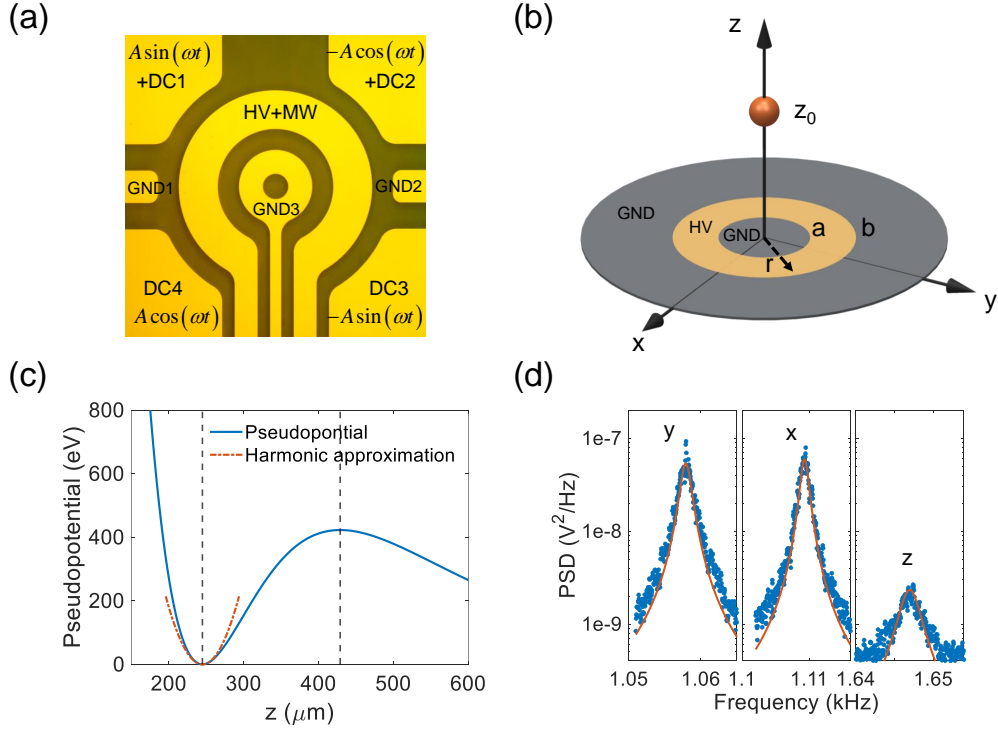
Supplementary Fig. 1 shows the schematic diagram of our experimental setup. The surface ion trap is fabricated on a sapphire wafer, which has a high transmittance for visible and near infrared laser. The chip is fixed on a 3D stage and installed in a vacuum chamber. The AC high voltage signal used to levitate nanodiamonds and the microwave used for quantum control are combined with a bias tee and delivered to the chip. A 532 nm laser beam is incident from the bottom to polarize a levitated nanodiamond. The photoluminescence (PL) is collected by an objective lens with a numerical aperture (NA) of 0.55. A 1064 nm laser beam focused by the same objective lens is used to monitor the center-of-mass (CoM) motion and the rotational motion of levitated nanodiamonds. The PL is separated with the 532 nm laser and the 1064 nm laser by two long-pass dichroic mirrors. The count rate and the optical spectrum of the PL are measured by a photon counter and a spectrometer. There are two cameras that monitor the procedure of particles loading and the trapping position of levitated nanoparticles.

Instead of a surface ring ion trap with concentric rings [64, 65], we use an Ω -shaped circuit to deliver both a high voltage for trapping and a microwave for controlling NV centers. A blank hole in the center allows the probing laser to travel through. The planar design conveniently provides six-directional detection. To theoretically calculate the trapping parameters, including the trapping position and the trapping depth, we approximate the homemade surface ion trap (Supplement Fig. 2(a)) as a perfect ring ion trap (Supplement Fig. 2(b)). The area $a \leq r \leq b$ is connected to an AC high voltage driving signal with a frequency of f_d and an amplitude of V_d , while the remaining parts are grounded. For a surface ion trap, the motion of particles in z axis (perpendicular to the chip surface) is more critical. The motion equation of a nanoparticle along the z axis can be approximately written as [64]:

$$m \frac{d^2 z}{dt^2} = -QV_d \cos(2\pi f_d t) f(a, b)(z - z_0), \quad (\text{A1})$$



Supplemental Fig. 1. Schematic diagram of the experimental setup. The surface ion trap is fixed on a 3D stage and installed in the vacuum chamber. A 532 nm laser beam controlled by an acousto-optic modulator (AOM) is incident from the bottom to excite diamond NV centers in a levitated nanodiamond. The photoluminescence (PL) is collected by an objective lens. A 1064 nm laser beam focused by the same objective lens is used to monitor the motion of levitated nanodiamonds. The PL is separated with the 532 nm laser and the 1064 nm laser by two long-pass dichroic mirrors (DMLP650 and DMLP1000). PBS: Polarizing beam splitter; $\lambda/2$: half-wave plate; $\lambda/4$: quarter-wave plate; BP: band-pass filters



Supplemental Fig. 2. Surface ion trap and CoM motion of a levitated nanodiamond. (a) Optical image of the surface ion trap. The outer four electrodes are used for compensation of residual charges on the chip surface. Trapping voltage and microwave can be delivered by a bias-tee simultaneously. (b) Equivalent surface ion trap with concentric rings design. Ring area $a \leq r \leq b$ is connected to an AC high voltage and the remaining parts are grounded. (c) Theoretical pseudopotential calculation in z axis of a concentric rings ion trap. The trapping position is located at $z_0 = 245 \mu\text{m}$ and the trapping depth is around 420 eV. The parameters used for this calculation are listed in Table I. (d) PSDs of the CoM motion of the levitated nanodiamond in three dimensions at the pressure of 0.01 Torr. The radius is about 264 nm by the Lorentzian fitting.

where m is the mass of the nanoparticle, Q is the charges, $z_0 = \sqrt{a^{4/3}b^{4/3}/(a^{2/3} + b^{2/3})}$ is the trapping position located at the zero field point, and $f(a, b)$ is the geometric factor given by

$$f(a, b) = \sqrt{\frac{9(b^{2/3} - a^{2/3})^2(b^{2/3} + a^{2/3})^6}{a^{4/3}b^{4/3}(a^{4/3} + a^{2/3}b^{2/3} + b^{4/3})^5}}. \quad (\text{A2})$$

Eq. A1 shares the same forms as Mathieu equation. The trapping eigenfrequency along z direction can be solved as:

$$\omega_z = \frac{q}{2\sqrt{2}} 2\pi f_d = \frac{QV_d}{2\sqrt{2}\pi m f_d} f(a, b). \quad (\text{A3})$$

For a regime with small displacement of a levitated nanodiamond, the electric potential can be approximated as a harmonic potential near the trapping region:

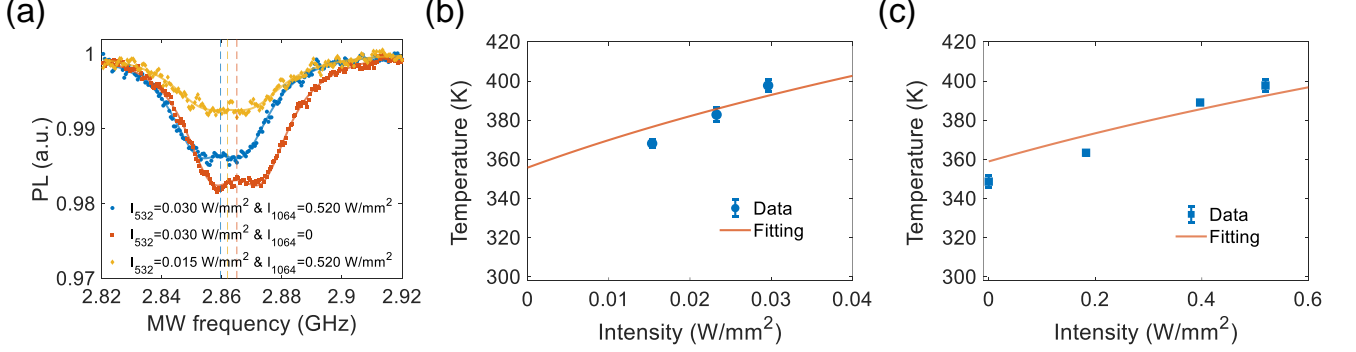
$$V_{\text{potential}}(z) = \frac{1}{2} m \omega_z^2 (z - z_0)^2 = \frac{Q^2 V_d^2}{16\pi^2 m f_d^2} f^2(a, b) (z - z_0)^2. \quad (\text{A4})$$

Generally, when the levitated nanodiamond moves away from the harmonic region, the pseudopotential can be written as [64]:

$$V_{\text{potential}}(z) = \frac{Q^2 V_d^2}{16\pi^2 m f_d^2} \left| \nabla \left(\frac{1}{\sqrt{1 + (a/z)^2}} - \frac{1}{\sqrt{1 + (b/z)^2}} \right) \right|^2. \quad (\text{A5})$$

Table I. Parameters for the pseudopotential calculation of equivalent surface ion trap. q_z satisfies the condition of stable 3D trapping.

Q/e	R/nm	$\rho/(\text{kg}/\text{m}^3)$	V_d/V	f_d/Hz	$a/\mu\text{m}$	$b/\mu\text{m}$	q_z
2000	264	3500	300	$2\pi \times 1.6 \times 10^4$	270	450	0.29



Supplemental Fig. 3. Internal temperature of a levitated nanodiamond. (a) ODMRs of the levitated nanodiamond at different intensities of the 532 nm laser and the 1064 nm laser at the pressure of 1.3×10^{-5} Torr. (b) Internal temperature as a function of the intensity of the 532 nm laser. The intensity of the 1064 nm laser is $0.520 \text{ W}/\text{mm}^2$. (c) Internal temperature as a function of the intensity of the 1064 nm laser. The intensity of the 532 nm laser is $0.030 \text{ W}/\text{mm}^2$.

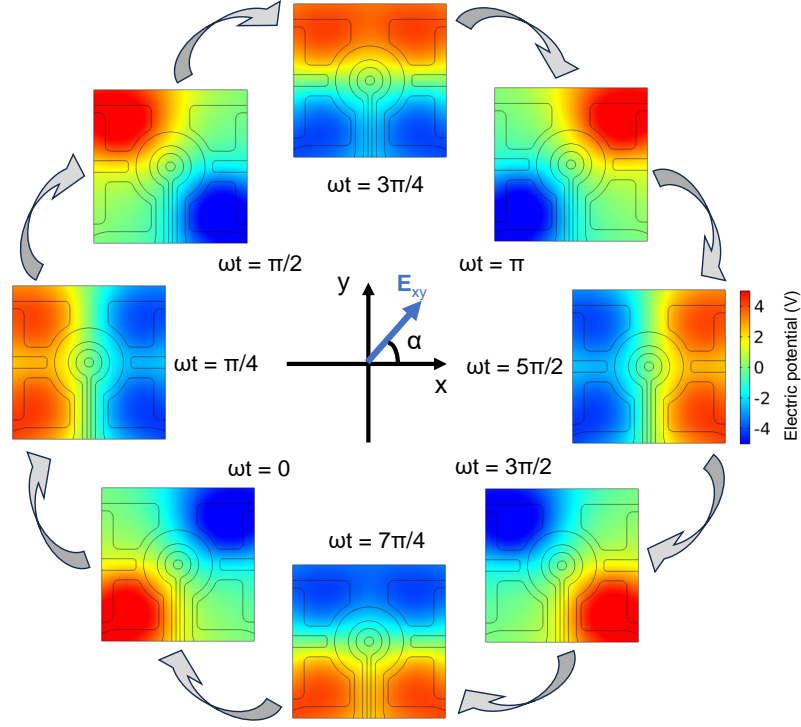
The dimension of the surface ion trap is designed as $a = 270 \mu\text{m}$ and $b = 450 \mu\text{m}$. We theoretically calculate the trapping potential of a levitated nanodiamond in z axis, as shown in Supplement Fig. 2(c). The red dash-dotted curve and blue solid curve are calculated by Eq. A4 and Eq. A5, respectively. All the parameters are summarized in Table I. The theoretical trapping position z_0 is $245 \mu\text{m}$, which is very close to the simulation result $253 \mu\text{m}$ for the current ion trap design. The difference is due to the asymmetric ion trap design.

The trapping potential is dependent on the eigenfrequency of a levitated particle, which is proportional to the charge to mass ratio (Q/m). Thus, it is necessary to increase the charge number carried on particles to achieve stable levitation in an ion trap. In our experiment, the diamond particles were purchased from Adamas Nano and the product model is MDNV1umHi10mg (1 micron Carboxylated Red Fluorescence, 1 mg/mL in DI Water, 3.5 ppm NV). These particles exhibit an average size of 750 nm. They are created by irradiating 2-3 MeV electrons on diamonds manufactured by static high-pressure, high-temperature (HPHT) synthesis and containing about 100 ppm of substitutional N. The nanodiamonds are first sprayed out by electrospray, which is supplied by a DC high voltage ($\sim 2 \text{ kV}$). Then the nanodiamonds are delivered to the trapping region of the surface ion trap with an extra linear Paul trap.

After a nanodiamond is trapped, we apply a 1064 nm laser to measure the CoM motion of the levitated nanodiamond. Supplementary Fig. 2(d) is the PSDs of the CoM motion in x, y, z directions at the pressure of 0.01 Torr. The radius of the levitated nanodiamond is obtained to be about 264 nm based on the fitting of the PSDs. The experimental trapping frequency in z direction is about $\omega_z/2\pi = 1.65 \text{ kHz}$. Using Eq. A3, the charge number is estimated to be about 2000 for this nanodiamond. The surface ion trap creates an extremely deep potential well of 420 eV (Supplementary Fig. 2(c)). According to our experimental results, the charge number of different levitated nanodiamonds varies from 1,000 to 10,000.

Appendix B: Internal temperature of a levitated nanodiamond

The heating by the 532 nm laser and the 1064 nm laser affects the stability of the levitated nanodiamond in vacuum. Here we measure the ODMRs of the levitated nanodiamond at different intensities of the 532 nm laser (I_{532}) and the 1064 nm laser (I_{1064}), as shown in Supplementary Fig. 3(a). The pressure is fixed to 1.3×10^{-5} Torr. First, we adjust the intensity of the 532 nm laser from $0.015 \text{ W}/\text{mm}^2$ to $0.03 \text{ W}/\text{mm}^2$, while keeping $I_{1064} = 0.520 \text{ W}/\text{mm}^2$. The internal temperature of the levitated nanodiamond is shown in Supplementary Fig. 3(b). Then we measure the temperature when the intensity of the 1064 nm laser is changed from 0 to $0.520 \text{ W}/\text{mm}^2$ while the intensity of the



Supplemental Fig. 4. Simulation of the rotating electric potential in xy -plane generated by the four electrodes. The rotation phase (ωt) of each figure is changed from 0 to 2π by the step of $\pi/4$, and the direction of corresponding electric field rotate following the rotation phase.

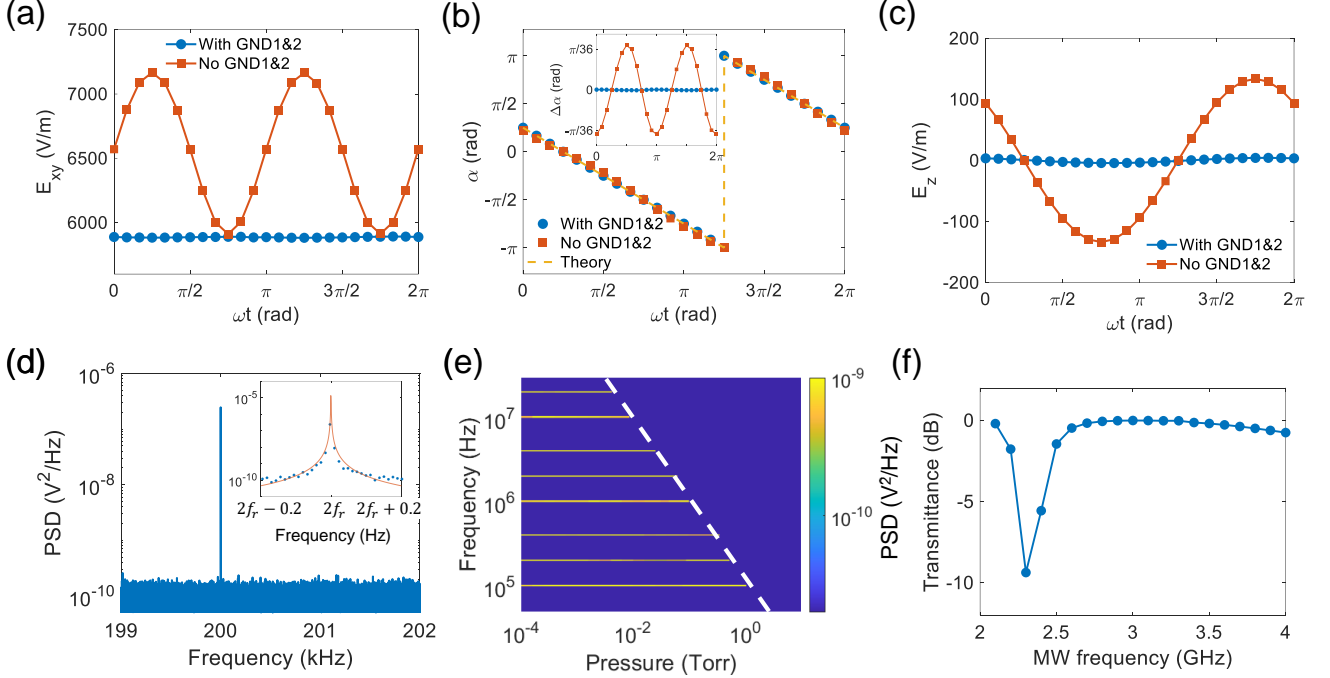
532 nm laser is fixed at $I_{532} = 0.03 \text{ W/mm}^2$ (Supplementary Fig. 3(c)). The red curves are the fittings by [51, 52]:

$$A_a = A_{gas}p(T - T_0) + A_{bb}(T^5 - T_0^5), \quad (\text{B1})$$

where the first term $A_a = \sum_{\lambda} \eta_{\lambda} I_{\lambda} V$ is the heating of the excitation laser ($\lambda = 532 \text{ nm}$) and the probe laser ($\lambda = 1064 \text{ nm}$), η_{λ} is the absorption coefficient of nanodiamond and I_{λ} is the laser intensity, V is the volume of nanodiamond. The second term is the cooling rate caused by gas molecule collisions, $A_{gas} = \frac{\kappa \pi R^2 v}{2T_0} \frac{\gamma' + 1}{\gamma' - 1}$, $\kappa \approx 1$ is the thermal accommodation coefficient of diamond, $R = 332 \text{ nm}$ is the radius of this nanodiamond (several different nanodiamonds are used in this experiment), v is the mean thermal speed of gas molecules, γ' is the specific heat ratio ($\gamma' = 7/5$ for air near room temperature), p is the pressure, T_0 is the thermal temperature (298 K). Plug in the parameters, we get the coefficient A_{gas} to be $1.74 \times 10^{-12} \text{ m}^3 \cdot \text{s}^{-1} \cdot \text{K}^{-1}$ for this nanodiamond. The last term is for cooling due to black-body radiation, where $A_{bb} = 72\zeta(5) V k_B^5 / (\pi^2 c^3 \hbar^4) \text{Im} \left(\frac{\varepsilon - 1}{\varepsilon + 2} \right)$, $\zeta(5) \approx 1.04$ is the Riemann zeta function, k_B is the Boltzmann constant, c is the vacuum light speed, \hbar is the reduced Planck's constant, ε is a constant and time-independent permittivity of nanodiamond across the black-body radiation spectrum. Based on the coefficient A_{gas} , we can calculate the absorption coefficients of 532 nm laser and 1064 nm laser to be 111 cm^{-1} and 5.87 cm^{-1} , respectively.

Appendix C: Rotation of a levitated nanodiamond driven by a rotating electric field

In our experiment, we use a rotating electric field to drive a levitated nanodiamond to rotate at high speed. The four electrodes at the corners are applied with 4 AC signals with the same frequency and amplitude but $\pi/2$ phase difference to generate a rotating electric field. The two grounded electrodes labeled by GND1 and GND2 (Supplementary Fig. 2(a)) are introduced to cancel the z component of the rotating electric field and make the electric field more symmetric. We simulate the electric fields for both the trapping potential and the rotating field using the COMSOL software. The simulation of the electric potential in xy -plane at different rotation phases are shown in Supplementary Fig. 4. The rotation phases are changed from 0 to 2π by steps of $\pi/4$ in the simulation. The dipole moment (\mathbf{p}) of a levitated



Supplemental Fig. 5. Simulation of the rotating electric field and the rotational motion of a levitated nanodiamond. Time evolution of the xy -plane component (a) and direction (b), z component (c) of the electric field with (blue circles) and without (red squares) the compensation electrodes of GND1 and GND2. α describes the orientation of the electric field ($\alpha = 0$ indicates the electric field points to positive x direction). (d) PSD of the rotational motion at the rotation frequency of 0.1 MHz. The linewidth is 9.9×10^{-5} Hz by the fitting (inset). The ratio of the center frequency to the linewidth is 2×10^9 . (e) PSDs of the rotational motion of the levitated nanodiamond at different pressures, showing the maximum rotation frequency at different pressures. The rotation frequencies are 0.05 MHz, 0.1 MHz, 0.2 MHz, 0.5 MHz, 1 MHz, 2 MHz, 5 MHz and 10 MHz, respectively. The upper limit of the rotation frequency is inversely proportional to pressure with the electric field driving. Particles stop rotating above the dashed white line. (f) Simulation of microwave transmittance of the surface ion trap.

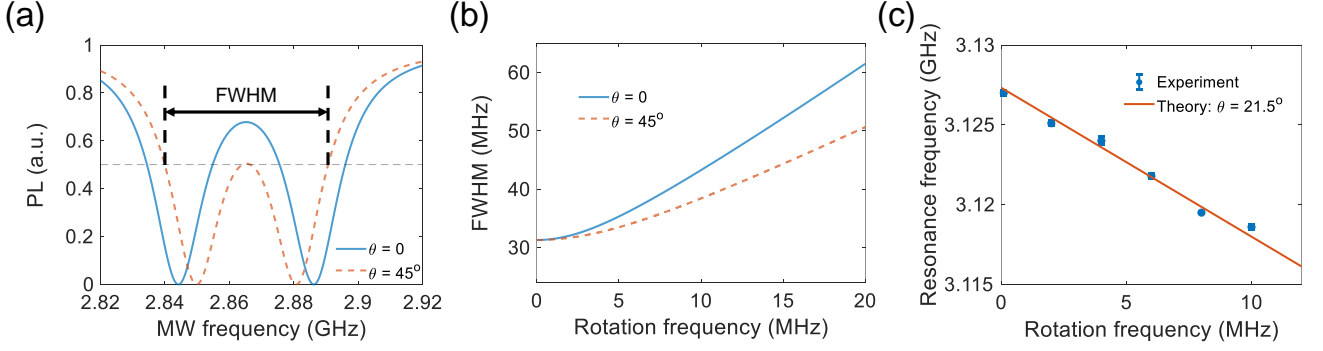
nanodiamond is aligned to the direction of the electric field (\mathbf{E}_{xy}) by the torque

$$\mathbf{M}_{electric} = \mathbf{p} \times \mathbf{E}_{xy} = |\mathbf{p}| |\mathbf{E}_{xy}| \sin \beta \cdot \mathbf{z}, \quad (\text{C1})$$

where β is the angle between the dipole moment and the electric field, \mathbf{z} is the unit vector along z direction.

Based on the simulation as shown in Supplementary Fig. 4, the amplitude and the direction (α) of the electric field in the xy -plane can be calculated, which is displayed in Supplementary Fig. 5(a) and 5(b). $\alpha = 0$ indicates that the rotating electric field points to the positive x direction. The blue circles and red squares are the simulations with and without the compensation electrodes GND 1 and GND 2. Ideally, the direction of the rotating electric field should be $\alpha(t) = \pi/4 - \omega t$ (orange dashed curve). The inset of Supplementary Fig. 5(b) is the asynchrony between the simulation result and an ideal rotation field with and without the compensation electrodes. The orientation of the electric field does not perfectly rotate at a constant speed in one period without the compensation electrodes (blue circles). The maximum deviation is 5.5° . It hurts the stability of the rotational motion of the levitated nanodiamonds and expand the linewidth of nanodiamond's rotation signal. Moreover, the E_z component of the rotating electrical field oscillates with a large amplitude if there are no compensation electrodes (Supplementary Fig. 5(c)). The electrical field drives a levitated nanodiamond to oscillate in the z direction, causing the loss of the levitated nanodiamond in high vacuum. The two compensation electrodes effectively solve these issues. The transmittance of a microwave through the Ω -shaped circuit is simulated (Supplementary Fig. 5(f)) to ensure the microwave has low loss for frequencies from 2.6 GHz to 3.1 GHz.

Then we drive a levitated nanodiamond to rotate using the rotating electric field. The PSD of the rotational motion at the rotation frequency of 0.1 MHz is shown in Supplementary Fig. 5(d). The linewidth of the rotation signal is about 9.9×10^{-5} Hz based on a Lorentzian fitting (inset of Supplementary Fig. 5(d)). Thus, the ratio of the center frequency to the linewidth is 2×10^9 , demonstrating the rotational motion is ultra-stable with easy control by this



Supplemental Fig. 6. Berry phase induced by a rotating nanodiamond. (a) Theoretically calculated ODMR of NV centers with different orientations at the rotation frequency of 20 MHz. The blue solid, red dashed and orange dash-dotted curves are calculated at $\theta = 0$ and $\theta = 45^\circ$, respectively. (b) Theoretically calculated FWHM of the ODMR as a function of rotation frequency. The blue solid curve and the red dashed curve are calculated for $\theta = 0$ and $\theta = 45^\circ$, respectively. (c) Experimental results of the frequency shift due to the Berry phase induced by counterclockwise rotation (blue circles), and theoretical calculated resonance frequency as a function of the rotation frequency at $\theta = 21.5^\circ$ (red curve).

method.

Meanwhile, the rotational motion of the levitated nanodiamond is damped by the interaction with the remaining gas molecules in vacuum chamber. The damping torque of a sphere is [20, 66]

$$M_{gas} = -I\omega_r\gamma_d, \quad (C2)$$

where I is the moment of inertia of the nanodiamond, ω_r is the angular velocity, $\gamma_d = 40\eta'pR^2/3mv$ is the damping rate of rotational motion, $\eta' \approx 1$ is the accommodation factor accounting for the efficiency of the angular momentum transferred onto the nanodiamond by gas molecule collisions. Thus, the rotational motion equation can be written as:

$$I \frac{d\omega_r}{dt} = M_{electric} + M_{gas}. \quad (C3)$$

The maximum rotation frequency of the levitated nanodiamonds is obtained at $M_{electric} = -M_{gas}$ and $\beta = \pi/2$, which is limited by the pressure in the vacuum chamber. The maximum rotation frequency at a certain pressure is:

$$\omega_{r \max} = |\mathbf{p}| |\mathbf{E}_{xy}| / I\gamma_d. \quad (C4)$$

We measure the upper limit of the rotation frequency at different pressures (Supplementary Fig. 5(e)). The PSDs as functions of air pressure are measured at the rotation frequencies of 0.05 MHz, 0.1 MHz, 0.2 MHz, 0.5 MHz, 1 MHz, 2 MHz, 5 MHz and 10 MHz. The levitated nanodiamond stops rotating when the pressure is too large for that rotation frequency. The maximum rotation frequency is inversely proportional to the pressure (white dashed curve). The dipole moment of the nanodiamond ($R = 264$ nm) is estimated to be about $|\mathbf{p}| = 3.13 \times 10^{-25}$ C·m (1.96 e· μ m). We can adjust and lock the rotation of the levitated nanodiamond at arbitrary frequency and pressure in the region below the white dashed curve. The maximum rotation frequency is $\omega_r = 2\pi \times 20$ MHz in this experiment, which is limited by the π -phase shifter (Mini-Circuits, ZFSCJ-2-2-S) used to generate the signals on the four electrodes. Under favorable conditions, the rotational motion can achieve a frequency exceeding 10 GHz at the pressure of 10^{-6} Torr based on the dashed line in Supplementary Fig. 5(e).

Appendix D: Berry phase of rotating NV electron spins

1. Without an external magnetic field

In a rotating diamond, the embedded NV centers follow the rotation of the particle with an angular frequency of ω_r . Considering an arbitrary NV center in a diamond at the time of t , the angle between the NV axis and z axis is θ , and the azimuth angle is $\phi(t) = \omega_r t$ relative to x axis. In the absence of an external magnetic field and neglecting

strain effects, the Hamiltonian of the rotating NV center in the laboratory frame can be written as [34]

$$H_{0,lab} = \frac{1}{\hbar} R(t) D S_z^2 R^\dagger(t) = \frac{1}{\hbar} e^{-i\phi S_z} e^{-i\theta S_y} D S_z^2 e^{i\theta S_y} e^{i\phi S_z} \\ = D \hbar \begin{pmatrix} \cos^2\theta + \frac{\sin^2\theta}{2} & \frac{e^{-i\phi} \cos\theta \sin\theta}{\sqrt{2}} & \frac{e^{-2i\phi} \sin^2\theta}{2} \\ \frac{e^{i\phi} \cos\theta \sin\theta}{\sqrt{2}} & \sin^2\theta & -\frac{e^{-i\phi} \cos\theta \sin\theta}{\sqrt{2}} \\ \frac{e^{2i\phi} \sin^2\theta}{2} & -\frac{e^{i\phi} \cos\theta \sin\theta}{\sqrt{2}} & \cos^2\theta + \frac{\sin^2\theta}{2} \end{pmatrix}, \quad (D1)$$

where D is the zero-field splitting, $R(t) = R_z(\phi(t)) R_y(\theta)$ is the rotation transformation, and $R_y(\theta) = \exp(-i\theta S_y)$ ($R_z(\phi) = \exp(-i\phi S_z)$) expresses the rotation of spin around the y (z) axis in terms of θ (ϕ), \mathbf{S} is the spin operator. The Hamiltonian possesses three eigenstates $|m_s, t\rangle_{lab} = R(t) |m_s, 0\rangle_{lab}$ ($m_s = 0, \pm 1$),

$$|1, t\rangle_{lab} = R(t) \begin{pmatrix} 1 \\ 0 \\ 0 \end{pmatrix} = \begin{pmatrix} e^{-i\phi} \cos^2 \frac{\theta}{2} \\ \frac{\sin\theta}{\sqrt{2}} \\ e^{i\phi} \sin^2 \frac{\theta}{2} \end{pmatrix} \\ |0, t\rangle_{lab} = R(t) \begin{pmatrix} 0 \\ 1 \\ 0 \end{pmatrix} = \begin{pmatrix} -\frac{e^{-i\phi} \sin\theta}{\sqrt{2}} \\ \cos\theta \\ \frac{e^{i\phi} \sin\theta}{\sqrt{2}} \end{pmatrix}. \quad (D2) \\ |-1, t\rangle_{lab} = R(t) \begin{pmatrix} 0 \\ 0 \\ 1 \end{pmatrix} = \begin{pmatrix} e^{-i\phi} \sin^2 \frac{\theta}{2} \\ -\frac{\sin\theta}{\sqrt{2}} \\ e^{i\phi} \cos^2 \frac{\theta}{2} \end{pmatrix}$$

For a quantum system in an eigenstate, the system remains in the eigenstate and acquires a phase factor during an adiabatic evolution of the Hamiltonian. This factor arises from both the state's time evolution and the variation of the eigenstate with the changing Hamiltonian. The second term specifically corresponds to the Berry phase. Hence, the expression for the time-dependent spin state is [57]

$$e^{i\gamma_{m_s}} e^{-iH_{0,lab}t/\hbar} |m_s, t\rangle_{lab} = e^{i\gamma_{m_s}} e^{-iH_{0,lab}t/\hbar} e^{-i\phi S_z} e^{-i\theta S_y} |m_s, 0\rangle_{lab}, \quad (D3)$$

where γ_{m_s} is the Berry phase. Here, the diamond particle rotates around the z axis with a constant θ , the Berry phase can be calculated as [57]

$$\gamma_{m_s} = i \int_0^t \langle m_s, t' | \frac{\partial}{\partial t'} |m_s, t'\rangle_{lab} dt' = m_s \omega_r t \cos\theta. \quad (D4)$$

The Berry phase of Eq. D4 is calculated for an open-path, which is gauge-dependent. However, for a closed loop, the Berry phase is gauge-invariant and can be expressed as $m_s [-2\pi(1 - \cos\theta)]$. The result is equivalent to Eq. D4 of $m_s (2\pi \cos\theta)$.

The spin state of the NV center is observed through the interaction with a microwave magnetic field. In our experiment, the direction of the microwave is in the yz -plane and forms a slight angle θ' relative to the z axis, resulting from the asymmetric design of the waveguide. The Hamiltonian of the microwave in the laboratory frame can be written as

$$H_{MW,lab} = g\mu_B B_{MW} \cos(\omega_{MW}t) (S_z \cos\theta' + S_y \sin\theta') = H_{MW,z,lab} + H_{MW,y,lab}, \quad (D5)$$

which contains two components, the longitudinal term $H_{MW,z,lab} = g\mu_B B_{MW} \cos(\omega_{MW}t) S_z \cos\theta'$ and the transverse term $H_{MW,y,lab} = g\mu_B B_{MW} \cos(\omega_{MW}t) S_y \sin\theta'$. First, we consider the longitudinal term $H_{MW,z,lab}$. The expected value of the spin states can be expressed as

$$\begin{aligned} & \langle \pm 1, t | e^{iH_{0,lab}t/\hbar} e^{-i\gamma_{\pm 1}} H_{MW,z,lab} e^{i\gamma_0} e^{-iH_{0,lab}t/\hbar} |0, t\rangle_{lab} \\ &= g\mu_B B_{MW} \cos(\omega_{MW}t) \cos\theta' \langle \pm 1, 0 | e^{i\theta S_y} e^{i\phi S_z} e^{iH_{0,lab}t/\hbar} e^{-i\gamma_{\pm 1}} S_z e^{i\gamma_0} e^{-iH_{0,lab}t/\hbar} e^{-i\phi S_z} e^{-i\theta S_y} |0, 0\rangle_{lab} \\ &= g\mu_B B_{MW} \cos(\omega_{MW}t) \cos\theta' e^{-i(\gamma_{\pm 1} - \gamma_0)} e^{i(E_{\pm 1} - E_0)t/\hbar} \langle \pm 1, 0 | e^{i\theta S_y} e^{i\phi S_z} S_z e^{-i\phi S_z} e^{-i\theta S_y} |0, 0\rangle_{lab} \\ &= \frac{1}{2} g\mu_B B_{MW} \cos\theta' (e^{i\omega_{MW}t} + e^{-i\omega_{MW}t}) e^{\mp i\omega_r t \cos\theta} e^{iDt} \langle \pm 1, 0 | e^{i\theta S_y} S_z e^{-i\theta S_y} |0, 0\rangle_{lab} \\ &= \frac{1}{2} g\mu_B B_{MW} \cos\theta' [e^{i(\omega_{MW} \mp \omega_r \cos\theta + D)t} + e^{i(-\omega_{MW} \mp \omega_r \cos\theta + D)t}] \langle \pm 1, 0 | e^{i\theta S_y} S_z e^{-i\theta S_y} |0, 0\rangle_{lab} \\ &\approx \frac{1}{2} g\mu_B B_{MW} \cos\theta' e^{i(-\omega_{MW} + D \mp \omega_r \cos\theta)t} \langle \pm 1, 0 | e^{i\theta S_y} S_z e^{-i\theta S_y} |0, 0\rangle_{lab} \end{aligned}, \quad (D6)$$

where the E_{m_s} is the corresponding eigenvalue of the Hamiltonian $H_{0,lab}$ for the spin state $|m_s, t\rangle$. According to Eq. D6, the transformation of spin states from $|m_s = 0\rangle_{lab}$ to $|m_s = \pm 1\rangle_{lab}$ can be driven by a microwave operating at the resonance frequency of $D \mp \omega_r \cos\theta$, where the frequency shift $\mp \omega_r \cos\theta$ is attributed to the Berry phase.

Regarding the second part of the Hamiltonian in the transverse direction, $H_{MW,y,lab}$, the interaction between the microwave and the spin states can be formulated as

$$\begin{aligned}
& {}_{lab} \langle \pm 1, t | e^{iH_{0,lab}t/\hbar} e^{-i\gamma_{\pm 1}} H_{MW,y,lab} e^{i\gamma_0} e^{-iH_{0,lab}t/\hbar} | 0, t \rangle_{lab} \\
&= g\mu_B B_{MW} \cos(\omega_{MW}t) \sin\theta' {}_{lab} \langle \pm 1, 0 | e^{i\theta S_y} e^{i\phi S_z} e^{iH_{0,lab}t/\hbar} e^{-i\gamma_{\pm 1}} S_y e^{i\gamma_0} e^{-iH_{0,lab}t/\hbar} e^{-i\phi S_z} e^{-i\theta S_y} | 0, 0 \rangle_{lab} \\
&= g\mu_B B_{MW} \cos(\omega_{MW}t) \sin\theta' e^{-i(\gamma_{\pm 1} - \gamma_0)} e^{i(E_{\pm 1} - E_0)t/\hbar} {}_{lab} \langle \pm 1, 0 | e^{i\theta S_y} e^{i\phi S_z} S_y e^{-i\phi S_z} e^{-i\theta S_y} | 0, 0 \rangle_{lab} \\
&= \frac{1}{2} g\mu_B B_{MW} \sin\theta' (e^{i\omega_{MW}t} + e^{-i\omega_{MW}t}) e^{\mp i\omega_r t \cos\theta} e^{iDt} \\
&\times {}_{lab} \langle \pm 1, 0 | e^{i\theta S_y} \frac{1}{2i} (S_+ e^{i\omega_r t} - S_- e^{-i\omega_r t}) e^{-i\theta S_y} | 0, 0 \rangle_{lab}
\end{aligned} \tag{D7}$$

The expected values are written as

$$\begin{aligned}
& {}_{lab} \langle +1, t | e^{iH_{0,lab}t/\hbar} e^{-i\gamma_{+1}} H_{MW,y,lab} e^{i\gamma_0} e^{-iH_{0,lab}t/\hbar} | 0, t \rangle_{lab} \\
&= \frac{1}{4i} g\mu_B B_{MW} \sin\theta' [e^{i(\omega_{MW} - \omega_r \cos\theta + D + \omega_r)t} + e^{i(-\omega_{MW} - \omega_r \cos\theta + D + \omega_r)t}] \\
&\times {}_{lab} \langle +1, 0 | e^{i\theta S_y} S_+ e^{-i\theta S_y} | 0, 0 \rangle_{lab} \\
&\approx \frac{1}{4i} g\mu_B B_{MW} \sin\theta' e^{i(-\omega_{MW} + D + \omega_r - \omega_r \cos\theta)t} {}_{lab} \langle +1, 0 | e^{i\theta S_y} S_+ e^{-i\theta S_y} | 0, 0 \rangle_{lab}
\end{aligned} \tag{D8}$$

$$\begin{aligned}
& {}_{lab} \langle -1, t | e^{iH_{0,lab}t/\hbar} e^{-i\gamma_{-1}} H_{MW,y,lab} e^{i\gamma_0} e^{-iH_{0,lab}t/\hbar} | 0, t \rangle_{lab} \\
&= -\frac{1}{4i} g\mu_B B_{MW} \sin\theta' [e^{i(\omega_{MW} + \omega_r \cos\theta + D - \omega_r)t} + e^{i(-\omega_{MW} + \omega_r \cos\theta + D - \omega_r)t}] \\
&\times {}_{lab} \langle -1, 0 | e^{i\theta S_y} S_- e^{-i\theta S_y} | 0, 0 \rangle_{lab} \\
&\approx -\frac{1}{4i} g\mu_B B_{MW} \sin\theta' e^{i(-\omega_{MW} + D - \omega_r + \omega_r \cos\theta)t} {}_{lab} \langle -1, 0 | e^{i\theta S_y} S_- e^{-i\theta S_y} | 0, 0 \rangle_{lab}
\end{aligned} \tag{D9}$$

Utilizing Eq. D8 and Eq. D9, the resonance frequency of microwave for transforming the spin state from $|m_s = 0\rangle_{lab}$ to $|m_s = \pm 1\rangle_{lab}$ is $D \pm \omega_r(1 - \cos\theta)$. In addition to the frequency shift of $\mp\omega_r \cos\theta$ caused by the Berry phase, there is another term of ω_r coming from the rotational Doppler effect [57]. In our experiment, the angle θ' of the microwave relate to the z axis is approximately 8.5° . Consequently, the dominant transition probability arises from the longitudinal component, characterized by a frequency shift of $\mp\omega_r \cos\theta$ due to the Berry phase.

The energy levels of NV centers with four orientations are degenerate in the absence of an external magnetic field. When the nanodiamond undergoes rotation, the electron spin resonance frequency experiences a shift due to the Berry phase, and this shift depends on the angle θ between the NV axis and the rotation axis. The electron spin resonance frequencies of NV spins along different orientations become non-degenerate. The ODMR of NV at different orientations are theoretically calculated by Eq. D6 at the rotation frequency of 20 MHz (Supplementary Fig. 6(a)). The orientations corresponding to the blue solid curve and the red dashed curve are $\theta = 0^\circ$ and $\theta = 45^\circ$, respectively. The intrinsic linewidth is $2\pi \times 19$ MHz, and the strain effect splitting E is $2\pi \times 6.7$ MHz. The eight dips are not separated in the ODMR spectrum at a rotation frequency of a few MHz because of the large linewidth. Here we use the FWHM parameter of the ODMR spectrum to indicate the frequency shift by the Berry phase of a rotating NV center. The FWHM of the ODMR is mainly determined by the splitting of the NV centers that have the smallest θ . Supplementary Fig. 6(b) shows the FWHM of the ODMR as a function of rotation frequency. The NV centers, which have the smallest θ , show the highest sensitivity of the frequency shift due to the Berry phase.

2. With an external magnetic field

To precisely measure the frequency shift induced by the Berry phase of a rotating NV center, an external magnetic field \mathbf{B} along the z direction can be applied. This serves to distinguish the energy levels of NV centers in four different orientations. The Hamiltonian of a NV center in the laboratory frame with the external magnetic field can be expressed as

$$\begin{aligned}
H_{lab} &= H_{0,lab} + g\mu_B B S_z = \frac{1}{\hbar} e^{-i\phi S_z} e^{-i\theta S_y} D S_z^2 e^{i\theta S_y} e^{i\phi S_z} + g\mu_B B S_z \\
&= D\hbar \begin{pmatrix} \cos^2\theta + \frac{\sin^2\theta}{2} + \frac{g\mu_B B}{D} & \frac{e^{-i\phi} \cos\theta \sin\theta}{\sqrt{2}} & \frac{e^{-2i\phi} \sin^2\theta}{2} \\ \frac{e^{i\phi} \cos\theta \sin\theta}{\sqrt{2}} & \sin^2\theta & -\frac{e^{-i\phi} \cos\theta \sin\theta}{\sqrt{2}} \\ \frac{e^{2i\phi} \sin^2\theta}{2} & -\frac{e^{i\phi} \cos\theta \sin\theta}{\sqrt{2}} & \cos^2\theta + \frac{\sin^2\theta}{2} - \frac{g\mu_B B}{D} \end{pmatrix}.
\end{aligned} \tag{D10}$$

In the rotating frame, the Hamiltonian of the NV center can be calculated by a unitary transformation,

$$\begin{aligned}
H_{rot} &= U H_{lab} U^\dagger + i\partial_t U U^\dagger = e^{i\theta S_y} e^{i\phi S_z} H_{lab} e^{-i\phi S_z} e^{-i\theta S_y} + i\partial_t e^{i\theta S_y} e^{i\phi S_z} e^{-i\phi S_z} e^{-i\theta S_y} \\
&= \hbar \begin{pmatrix} D + g\mu_B B \cos\theta & -\frac{g\mu_B B \sin\theta}{\sqrt{2}} & 0 \\ -\frac{g\mu_B B \sin\theta}{\sqrt{2}} & 0 & -\frac{g\mu_B B \sin\theta}{\sqrt{2}} \\ 0 & -\frac{g\mu_B B \sin\theta}{\sqrt{2}} & D - g\mu_B B \cos\theta \end{pmatrix} + \hbar \begin{pmatrix} -\omega_r \cos\theta & \frac{\omega_r \sin\theta}{\sqrt{2}} & 0 \\ \frac{\omega_r \sin\theta}{\sqrt{2}} & 0 & \frac{\omega_r \sin\theta}{\sqrt{2}} \\ 0 & \frac{\omega_r \sin\theta}{\sqrt{2}} & \omega_r \cos\theta \end{pmatrix},
\end{aligned} \tag{D11}$$

where the unitary operator is defined as $U = e^{i\theta S_y} e^{i\phi S_z}$. The second term on the right side of Eq. D11 represents Zeeman interaction arising from the pseudo-magnetic field due to the rotation of the NV center. In the case of an adiabatic process, $\omega_r \ll D - g\mu_B B \cos \theta$, the second term is significantly weaker than the first term, and can be treated as a perturbation. We neglect the off-diagonal terms in the first component since $g\mu_B B \ll D$, which are too small to induce significant mixing of the NV spin states.

$$H_{rot} \approx \hbar \begin{pmatrix} D + g\mu_B B \cos \theta & 0 & 0 \\ 0 & 0 & 0 \\ 0 & 0 & D - g\mu_B B \cos \theta \end{pmatrix} + \hbar \begin{pmatrix} -\omega_r \cos \theta & \frac{\omega_r \sin \theta}{\sqrt{2}} & 0 \\ \frac{\omega_r \sin \theta}{\sqrt{2}} & 0 & \frac{\omega_r \sin \theta}{\sqrt{2}} \\ 0 & \frac{\omega_r \sin \theta}{\sqrt{2}} & \omega_r \cos \theta \end{pmatrix}. \quad (\text{D12})$$

Therefore, the Hamiltonian in the rotating frame possesses three eigenstates, $|m_s\rangle_{rot}$ ($m_s = 0, \pm 1$):

$$\begin{aligned} | +1 \rangle_{rot} &= \begin{pmatrix} 1 \\ 0 \\ 0 \end{pmatrix} \\ | 0 \rangle_{rot} &= \begin{pmatrix} 0 \\ 1 \\ 0 \end{pmatrix}, \\ | -1 \rangle_{rot} &= \begin{pmatrix} 0 \\ 0 \\ 1 \end{pmatrix} \end{aligned} \quad (\text{D13})$$

and the corresponding eigenvalues are $\hbar(D + g\mu_B B \cos \theta)$, 0, $\hbar(D - g\mu_B B \cos \theta)$, respectively. The new Hamiltonian in the laboratory frame can be transformed by applying the rotation transformation $R(t) = e^{-i\phi S_z} e^{-i\theta S_y}$,

$$\begin{aligned} H_{lab} &= RH_{rot}R^\dagger + i\partial_t RR^\dagger = e^{-i\phi S_z} e^{-i\theta S_y} H_{rot} e^{i\theta S_y} e^{i\phi S_z} + i\partial_t e^{-i\phi S_z} e^{-i\theta S_y} e^{i\theta S_y} e^{i\phi S_z} \\ &= \hbar \begin{pmatrix} D \frac{1+\cos^2 \theta}{2} + g\mu_B B \cos^2 \theta & \frac{e^{-i\phi} (D+g\mu_B B) \cos \theta \sin \theta}{\sqrt{2}} & \frac{e^{-2i\phi} D \sin^2 \theta}{2} \\ \frac{e^{i\phi} (D+g\mu_B B) \cos \theta \sin \theta}{\sqrt{2}} & D \sin^2 \theta & -\frac{e^{-i\phi} (D-g\mu_B B) \cos \theta \sin \theta}{\sqrt{2}} \\ \frac{e^{2i\phi} D \sin^2 \theta}{2} & -\frac{e^{i\phi} (D-g\mu_B B) \cos \theta \sin \theta}{\sqrt{2}} & D \frac{1+\cos^2 \theta}{2} - g\mu_B B \cos^2 \theta \end{pmatrix}. \end{aligned} \quad (\text{D14})$$

The eigenstates of the Hamiltonian in the laboratory frame also can be calculated through the rotation transformation,

$$\begin{aligned} | +1, t \rangle_{lab} &= R(t) | +1 \rangle_{rot} = \begin{pmatrix} e^{-i\phi} \cos^2 \frac{\theta}{2} \\ \frac{\sin \theta}{\sqrt{2}} \\ e^{i\phi} \sin^2 \frac{\theta}{2} \end{pmatrix} \\ | 0, t \rangle_{lab} &= R(t) | 0 \rangle_{rot} = \begin{pmatrix} -\frac{e^{-i\phi} \sin \theta}{\sqrt{2}} \\ \cos \theta \\ \frac{e^{i\phi} \sin \theta}{\sqrt{2}} \end{pmatrix}, \\ | -1, t \rangle_{lab} &= R(t) | -1 \rangle_{rot} = \begin{pmatrix} e^{-i\phi} \sin^2 \frac{\theta}{2} \\ -\frac{\sin \theta}{\sqrt{2}} \\ e^{i\phi} \cos^2 \frac{\theta}{2} \end{pmatrix} \end{aligned} \quad (\text{D15})$$

which are same as the eigenstates of the Hamiltonian without the external magnetic field (Eq. D2). Thus, the Berry phase of the rotating NV center is:

$$\gamma_{m_s} = m_s \omega_r t \cos \theta \quad (\text{D16})$$

Similarly, the interaction between microwave and the time-dependent spin states is still divided into two components. For the longitudinal component, it can be expressed as

$$\begin{aligned} &{}_{lab} \langle \pm 1, t | e^{iH_{lab}t/\hbar} e^{-i\gamma_{\pm 1}} H_{MW,z,lab} e^{i\gamma_0} e^{-iH_{lab}t/\hbar} | 0, t \rangle_{lab} \\ &= g\mu_B B_{MW} \cos(\omega_{MW}t) \cos \theta' {}_{lab} \langle \pm 1, 0 | e^{i\theta S_y} e^{i\phi S_z} e^{iH_{lab}t/\hbar} e^{-i\gamma_{\pm 1}} S_z e^{i\gamma_0} e^{-iH_{lab}t/\hbar} e^{-i\phi S_z} e^{-i\theta S_y} | 0, 0 \rangle_{lab} \\ &= g\mu_B B_{MW} \cos(\omega_{MW}t) \cos \theta' e^{-i(\gamma_{\pm 1} - \gamma_0)} e^{i(E_{B,\pm 1} - E_{B,0})t/\hbar} {}_{lab} \langle \pm 1, 0 | e^{i\theta S_y} e^{i\phi S_z} S_z e^{-i\phi S_z} e^{-i\theta S_y} | 0, 0 \rangle_{lab} \\ &= \frac{1}{2} g\mu_B B_{MW} \cos \theta' (e^{i\omega_{MW}t} + e^{-i\omega_{MW}t}) e^{\mp i\omega_r t \cos \theta} e^{i(D \pm g\mu_B B \cos \theta)t} {}_{lab} \langle \pm 1, 0 | e^{i\theta S_y} S_z e^{-i\theta S_y} | 0, 0 \rangle_{lab} \\ &= \frac{1}{2} g\mu_B B_{MW} \cos \theta' [e^{i(\omega_{MW} \mp \omega_r \cos \theta + D \pm g\mu_B B \cos \theta)t} + e^{i(-\omega_{MW} \mp \omega_r \cos \theta + D \pm g\mu_B B \cos \theta)t}] \\ &\times {}_{lab} \langle \pm 1, 0 | e^{i\theta S_y} S_z e^{-i\theta S_y} | 0, 0 \rangle_{lab} \\ &\approx \frac{1}{2} g\mu_B B_{MW} \cos \theta' e^{i(-\omega_{MW} + D \pm g\mu_B B \cos \theta \mp \omega_r \cos \theta)t} {}_{lab} \langle \pm 1, 0 | e^{i\theta S_y} S_z e^{-i\theta S_y} | 0, 0 \rangle_{lab} \end{aligned} \quad (\text{D17})$$

where the E_{B,m_s} is the eigenvalue of the Hamiltonian H_{lab} for the spin state $|m_s, t\rangle_{lab}$. The spin resonance frequency, transformed from $|m_s = 0\rangle_{lab}$ to $|m_s = \pm 1\rangle_{lab}$ is $D \pm g\mu_B B \cos \theta \mp \omega_r \cos \theta$. The frequency shift due to the Berry phase is $\mp \omega_r \cos \theta$.

The transverse component can be expressed as

$$\begin{aligned}
& {}_{lab} \langle \pm 1, t | e^{iH_{lab}t/\hbar} e^{-i\gamma_{\pm 1}} H_{MW,y,lab} e^{i\gamma_0} e^{-iH_{lab}t/\hbar} | 0, t \rangle_{lab} \\
&= g\mu_B B_{MW} \cos(\omega_{MW}t) \sin \theta' {}_{lab} \langle \pm 1, 0 | e^{i\theta S_y} e^{i\phi S_z} e^{iH_{lab}t/\hbar} e^{-i\gamma_{\pm 1}} S_y e^{i\gamma_0} e^{-iH_{lab}t/\hbar} e^{-i\phi S_z} e^{-i\theta S_y} | 0, 0 \rangle_{lab} \\
&= g\mu_B B_{MW} \cos(\omega_{MW}t) \sin \theta' e^{-i(\gamma_{\pm 1} - \gamma_0)} e^{i(E_{B,\pm 1} - E_{B,0})t/\hbar} {}_{lab} \langle \pm 1, 0 | e^{i\theta S_y} e^{i\phi S_z} S_y e^{-i\phi S_z} e^{-i\theta S_y} | 0, 0 \rangle_{lab} \cdot \\
&= \frac{1}{2} g\mu_B B_{MW} \sin \theta' (e^{i\omega_{MW}t} + e^{-i\omega_{MW}t}) e^{\mp i\omega_r t \cos \theta} e^{i(D \pm g\mu_B B \cos \theta)t} \\
&\times {}_{lab} \langle \pm 1, 0 | e^{i\theta S_y} \frac{1}{2i} (S_+ e^{i\omega_r t} - S_- e^{-i\omega_r t}) e^{-i\theta S_y} | 0, 0 \rangle_{lab}
\end{aligned} \tag{D18}$$

The expected values are written as

$$\begin{aligned}
& {}_{lab} \langle +1, t | e^{iH_{lab}t/\hbar} e^{-i\gamma_{+1}} H_{MW,y,lab} e^{i\gamma_0} e^{-iH_{lab}t/\hbar} | 0, t \rangle_{lab} \\
&= \frac{1}{4i} g\mu_B B_{MW} \sin \theta' [e^{i(\omega_{MW} - \omega_r \cos \theta + D + g\mu_B B \cos \theta + \omega_r)t} + e^{i(-\omega_{MW} - \omega_r \cos \theta + D + g\mu_B B \cos \theta + \omega_r)t}] \\
&\times {}_{lab} \langle +1, 0 | e^{i\theta S_y} S_+ e^{-i\theta S_y} | 0, 0 \rangle_{lab} \\
&\approx \frac{1}{4i} g\mu_B B_{MW} \sin \theta' e^{i(-\omega_{MW} - \omega_r \cos \theta + D + g\mu_B B \cos \theta + \omega_r)t} {}_{lab} \langle +1, 0 | e^{i\theta S_y} S_+ e^{-i\theta S_y} | 0, 0 \rangle_{lab}
\end{aligned} \tag{D19}$$

$$\begin{aligned}
& {}_{lab} \langle -1, t | e^{iH_{lab}t/\hbar} e^{-i\gamma_{-1}} H_{MW,y,lab} e^{i\gamma_0} e^{-iH_{lab}t/\hbar} | 0, t \rangle_{lab} \\
&= -\frac{1}{4i} g\mu_B B_{MW} \sin \theta' [e^{i(\omega_{MW} + \omega_r \cos \theta + D - g\mu_B B \cos \theta - \omega_r)t} + e^{i(-\omega_{MW} + \omega_r \cos \theta + D - g\mu_B B \cos \theta - \omega_r)t}] \\
&\times {}_{lab} \langle -1, 0 | e^{i\theta S_y} S_- e^{-i\theta S_y} | 0, 0 \rangle_{lab} \\
&\approx -\frac{1}{4i} g\mu_B B_{MW} \sin \theta' e^{i(-\omega_{MW} + \omega_r \cos \theta + D - g\mu_B B \cos \theta - \omega_r)t} {}_{lab} \langle -1, 0 | e^{i\theta S_y} S_- e^{-i\theta S_y} | 0, 0 \rangle_{lab}
\end{aligned} \tag{D20}$$

The transformation resonance frequency is $D \pm g\mu_B B \cos \theta \pm \omega_r (1 - \cos \theta)$ between the $|m_s = 0\rangle_{lab}$ state and $|m_s = \pm 1\rangle_{lab}$ state. The corresponding frequency shift due to the Berry phase also is $\pm \omega_r \cos \theta$, and the frequency shift induced by the rotational Doppler effect is ω_r . Similar to the case of zero external magnetic field, the predominant transition probability arises from the longitudinal component, characterized by a frequency shift of $\mp \omega_r \cos \theta$ due to the Berry phase.

Supplementary Fig. 6(c) shows the frequency shift induced by the Berry phase in a levitated nanodiamond rotating counterclockwise (viewed from the positive z direction unless otherwise specified). The external magnetic field along the z direction is about 100 G. The resonance frequency transition between $|m_s = 0\rangle_{lab}$ state and $|m_s = +1\rangle_{lab}$ state decreases with an increasing of the rotation frequency, in contrast to the behavior observed in the levitated nanodiamond rotating clockwise. The red curve is the theoretical calculation for the angle of $\theta = 21.5^\circ$ between the NV axis and the rotating axis. The experimental data is in excellent agreement with the theoretical calculation, suggesting a consistent orientation of the NV centers at various rotation frequencies.

3. Pseudo-magnetic field due to rotation

The Berry phase observed in the laboratory frame is equivalent to the pseudo-magnetic field (called the Barnett field in [57]) in the rotational frame. In our experiment, the microwave source is fixed in the laboratory frame. Only the levitated nanodiamond is rotating. Thus, we observe the effect of the Berry phase [57]. It will be beneficial to also consider this system in the rotational frame. The electron spin resonance frequency shift of the rotating NV center involves the combination of the pseudo-magnetic field and the rotational Doppler effect in the rotating frame. As expressed in Eq. D11, the Hamiltonian of the pseudo-magnetic field in the rotating frame, induced by the rotation of a diamond particle, can be given by

$$H_{\omega_r} = \hbar \begin{pmatrix} -\omega_r \cos \theta & \frac{\omega_r \sin \theta}{\sqrt{2}} & 0 \\ \frac{\omega_r \sin \theta}{\sqrt{2}} & 0 & \frac{\omega_r \sin \theta}{\sqrt{2}} \\ 0 & \frac{\omega_r \sin \theta}{\sqrt{2}} & \omega_r \cos \theta \end{pmatrix} \approx \hbar \begin{pmatrix} -\omega_r \cos \theta & 0 & 0 \\ 0 & 0 & 0 \\ 0 & 0 & \omega_r \cos \theta \end{pmatrix}, \tag{D21}$$

where the off-diagonal terms also can be ignored. So the Hamiltonian of the NV center in the rotating frame can be expressed as

$$H_{rot} = \hbar \begin{pmatrix} D + g\mu_B B \cos \theta - \omega_r \cos \theta & 0 & 0 \\ 0 & 0 & 0 \\ 0 & 0 & D - g\mu_B B \cos \theta + \omega_r \cos \theta \end{pmatrix}. \tag{D22}$$

The corresponding eigenvalues are $\hbar(D + g\mu_B B \cos \theta - \omega_r \cos \theta)$, 0, $\hbar(D - g\mu_B B \cos \theta + \omega_r \cos \theta)$ for spin state $|+1\rangle_{rot}$, $|0\rangle_{rot}$ and $|-1\rangle_{rot}$, respectively.

The Hamiltonian describing the interaction of the microwave term with the NV center in the rotating frame can be expressed as

$$\begin{aligned} H_{MW,rot} &= U H_{MW,lab} U^\dagger = e^{i\theta S_y} e^{i\phi S_z} H_{MW,lab} e^{-i\phi S_z} e^{-i\theta S_y} \\ &= g\mu_B B_{MW} \cos(\omega_{MW} t) e^{i\theta S_y} e^{i\phi S_z} (S_z \cos \theta' + S_y \sin \theta') e^{-i\phi S_z} e^{-i\theta S_y} = H_{MW,z,rot} + H_{MW,y,rot} \end{aligned} \quad (D23)$$

where the longitudinal component is $H_{MW,z,rot} = g\mu_B B_{MW} \cos(\omega_{MW} t) e^{i\theta S_y} e^{i\phi S_z} S_z \cos \theta' e^{-i\phi S_z} e^{-i\theta S_y}$, and the transverse component is $H_{MW,y,rot} = g\mu_B B_{MW} \cos(\omega_{MW} t) e^{i\theta S_y} e^{i\phi S_z} S_y \sin \theta' e^{-i\phi S_z} e^{-i\theta S_y}$. The expected value of the spin state, interacting with the longitudinal component of microwave, can be expressed as

$$\begin{aligned} &{}_{rot} \langle \pm 1 | e^{iH_{rot}t/\hbar} H_{MW,z,rot} e^{-iH_{rot}t/\hbar} | 0 \rangle_{rot} \\ &= g\mu_B B_{MW} \cos \theta' \cos(\omega_{MW} t) {}_{rot} \langle \pm 1 | e^{iH_{rot}t/\hbar} e^{i\theta S_y} e^{i\phi S_z} S_z e^{-i\phi S_z} e^{-i\theta S_y} e^{-iH_{rot}t/\hbar} | 0 \rangle_{rot} \\ &= g\mu_B B_{MW} \cos \theta' \cos(\omega_{MW} t) e^{i(E_{\pm 1,rot} - E_{0,rot})t/\hbar} {}_{rot} \langle \pm 1 | e^{i\theta S_y} e^{i\phi S_z} S_z e^{-i\phi S_z} e^{-i\theta S_y} | 0 \rangle_{rot} \\ &= \frac{1}{2} g\mu_B B_{MW} \cos \theta' (e^{i\omega_{MW} t} + e^{-i\omega_{MW} t}) e^{i(D \pm g\mu_B B \cos \theta \mp \omega_r \cos \theta)t} {}_{rot} \langle \pm 1 | e^{i\theta S_y} S_z e^{-i\theta S_y} | 0 \rangle_{rot} \\ &= \frac{1}{2} g\mu_B B_{MW} \cos \theta' [e^{i(\omega_{MW} + D \pm g\mu_B B \cos \theta \mp \omega_r \cos \theta)t} + e^{i(-\omega_{MW} + D \pm g\mu_B B \cos \theta \mp \omega_r \cos \theta)t}] \\ &\times {}_{rot} \langle \pm 1 | e^{i\theta S_y} S_z e^{-i\theta S_y} | 0 \rangle_{rot} \\ &\approx \frac{1}{2} g\mu_B B_{MW} \cos \theta' e^{i(-\omega_{MW} + D \pm g\mu_B B \cos \theta \mp \omega_r \cos \theta)t} {}_{rot} \langle \pm 1 | e^{i\theta S_y} S_z e^{-i\theta S_y} | 0 \rangle_{rot} \end{aligned} \quad (D24)$$

where the $E_{m_s,rot}$ is the eigenvalue of the Hamiltonian H_{rot} for the spin state $|m_s\rangle_{rot}$ in the rotating frame. The transformation resonance frequency is $D \pm g\mu_B B \cos \theta \mp \omega_r \cos \theta$, and the last term $\mp \omega_r \cos \theta$ is the frequency shift due to the pseudo-magnetic field. The transverse component can be expressed as

$$\begin{aligned} &{}_{rot} \langle \pm 1 | e^{iH_{rot}t/\hbar} H_{MW,y,rot} e^{-iH_{rot}t/\hbar} | 0 \rangle_{rot} \\ &= g\mu_B B_{MW} \sin \theta' \cos(\omega_{MW} t) {}_{rot} \langle \pm 1 | e^{iH_{rot}t/\hbar} e^{i\theta S_y} e^{i\phi S_z} S_y e^{-i\phi S_z} e^{-i\theta S_y} e^{-iH_{rot}t/\hbar} | 0 \rangle_{rot} \\ &= g\mu_B B_{MW} \sin \theta' \cos(\omega_{MW} t) e^{i(E_{\pm 1,rot} - E_{0,rot})t/\hbar} {}_{rot} \langle \pm 1 | e^{i\theta S_y} e^{i\phi S_z} S_y e^{-i\phi S_z} e^{-i\theta S_y} | 0 \rangle_{rot} \\ &= \frac{1}{2} g\mu_B B_{MW} \sin \theta' (e^{i\omega_{MW} t} + e^{-i\omega_{MW} t}) e^{i(D \pm g\mu_B B \cos \theta \mp \omega_r \cos \theta)t} \\ &\times {}_{rot} \langle \pm 1 | e^{i\theta S_y} \frac{1}{2i} (S_+ e^{i\omega_r t} - S_- e^{-i\omega_r t}) e^{-i\theta S_y} | 0 \rangle_{rot} \end{aligned} \quad (D25)$$

The expected values are written as

$$\begin{aligned} &{}_{rot} \langle +1 | e^{iH_{rot}t/\hbar} H_{MW,y,rot} e^{-iH_{rot}t/\hbar} | 0 \rangle_{rot} \\ &= \frac{1}{4i} g\mu_B B_{MW} \sin \theta' [e^{i(\omega_{MW} + D + g\mu_B B \cos \theta - \omega_r \cos \theta + \omega_r)t} + e^{i(-\omega_{MW} + D + g\mu_B B \cos \theta - \omega_r \cos \theta + \omega_r)t}] \\ &\times {}_{rot} \langle +1 | e^{i\theta S_y} S_+ e^{-i\theta S_y} | 0 \rangle_{rot} \\ &\approx \frac{1}{4i} g\mu_B B_{MW} \sin \theta' e^{i(-\omega_{MW} + D + g\mu_B B \cos \theta - \omega_r \cos \theta + \omega_r)t} {}_{rot} \langle +1 | e^{i\theta S_y} S_+ e^{-i\theta S_y} | 0 \rangle_{rot} \end{aligned} \quad (D26)$$

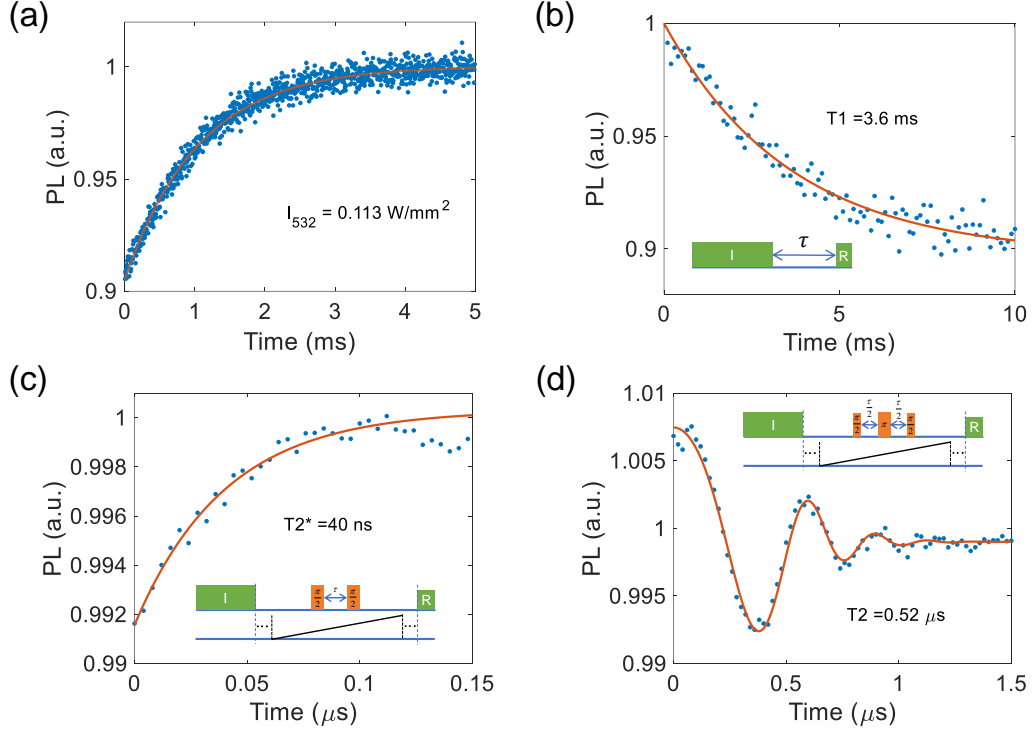
$$\begin{aligned} &{}_{rot} \langle -1 | e^{iH_{rot}t/\hbar} H_{MW,y,rot} e^{-iH_{rot}t/\hbar} | 0 \rangle_{rot} \\ &= -\frac{1}{4i} g\mu_B B_{MW} \sin \theta' [e^{i(\omega_{MW} + D - g\mu_B B \cos \theta + \omega_r \cos \theta - \omega_r)t} + e^{i(-\omega_{MW} + D - g\mu_B B \cos \theta + \omega_r \cos \theta - \omega_r)t}] \\ &\times {}_{rot} \langle -1 | e^{i\theta S_y} S_- e^{-i\theta S_y} | 0 \rangle_{rot} \\ &\approx -\frac{1}{4i} g\mu_B B_{MW} \sin \theta' e^{i(-\omega_{MW} + D - g\mu_B B \cos \theta + \omega_r \cos \theta - \omega_r)t} {}_{rot} \langle +1 | e^{i\theta S_y} S_+ e^{-i\theta S_y} | 0 \rangle_{rot} \end{aligned} \quad (D27)$$

The transformation resonance frequency between the $|m_s = 0\rangle_{rot}$ state and $|m_s = \pm 1\rangle_{rot}$ state is $D \pm g\mu_B B \cos \theta \pm \omega_r (1 - \cos \theta)$. The frequency shift of $\pm \omega_r (1 - \cos \theta)$ is induced by both the pseudo-magnetic field and the rotational Doppler effect [57] in the rotating frame.

Appendix E: Quantum measurement of levitated diamond NV centers

The power of 532 nm laser for NV initialization is very weak to minimize laser heating in high vacuum, leading to a long NV polarization time. The measured initialization time, shown in Supplementary Fig. 7(a), is 1.05 ms at the 532 nm laser intensity of 0.113 W/mm². We measure the spin relaxation time (T_1) of the levitated nanodiamond in Supplementary Fig. 7(c), indicating $T_1 = 3.60$ ms. It is three times longer than the initialization time. The T_2^* and T_2 are measured, as shown in Supplementary Fig. 7(c) and (d). The T_2^* is 40 ns and the T_2 is 0.52 μ s. In the spin echo measurement, the oscillation is a result of the misalignment of the magnetic field with the rotation axis [67].

Due to the Ω -shape design of the microwave antenna, the orientation of the magnetic component of microwave is located in yz -plane and slightly away from the z axis with an angle about $\theta' = 8.5^\circ$. Thus, the effective magnetic field



Supplemental Fig. 7. Quantum measurement of NV centers in a levitated nanodiamond. (a) Initialization time of levitated NV centers when the 532 nm laser intensity is 0.113 W/mm^2 . The initialization time is 1.05 ms. (b) Experimental result of T_1 measurement of the levitated nanodiamond. The insert is the sequence of T_1 measurement. The T_1 is 3.6 ms. (c) Ramsey measurement and its corresponding sequence with a T_2^* of 40 ns. (d) Spin Echo measurement and its corresponding sequence with a T_2 of $0.52 \mu\text{s}$. The oscillation is induced by the misalignment of the magnetic field with the rotation axis. In the sequences, the green and orange regions represent the pulses of the 532 nm laser and the microwave, respectively. The black lines are the rotation phase.

B_{MW}^\perp of the microwave acting on NV spins keeps varying at different rotation phase $\phi(t)$ of the levitated nanodiamond. We set the direction of a NV spin to be $\mathbf{n}_{NV} = (\sin \theta, 0, \cos \theta)$ in the xz -plane at initial time ($t = 0$), and then rotate it around the z axis. The rotation matrix is:

$$\mathbf{r}_z = \begin{pmatrix} \cos \phi(t) & -\sin \phi(t) & 0 \\ \sin \phi(t) & \cos \phi(t) & 0 \\ 0 & 0 & 1 \end{pmatrix}. \quad (\text{E1})$$

After a rotation time of t , the direction of the NV spin is changed to

$$\mathbf{n}'_{NV} = (\cos \phi(t) \sin \theta, \sin \phi(t) \sin \theta, \cos \theta). \quad (\text{E2})$$

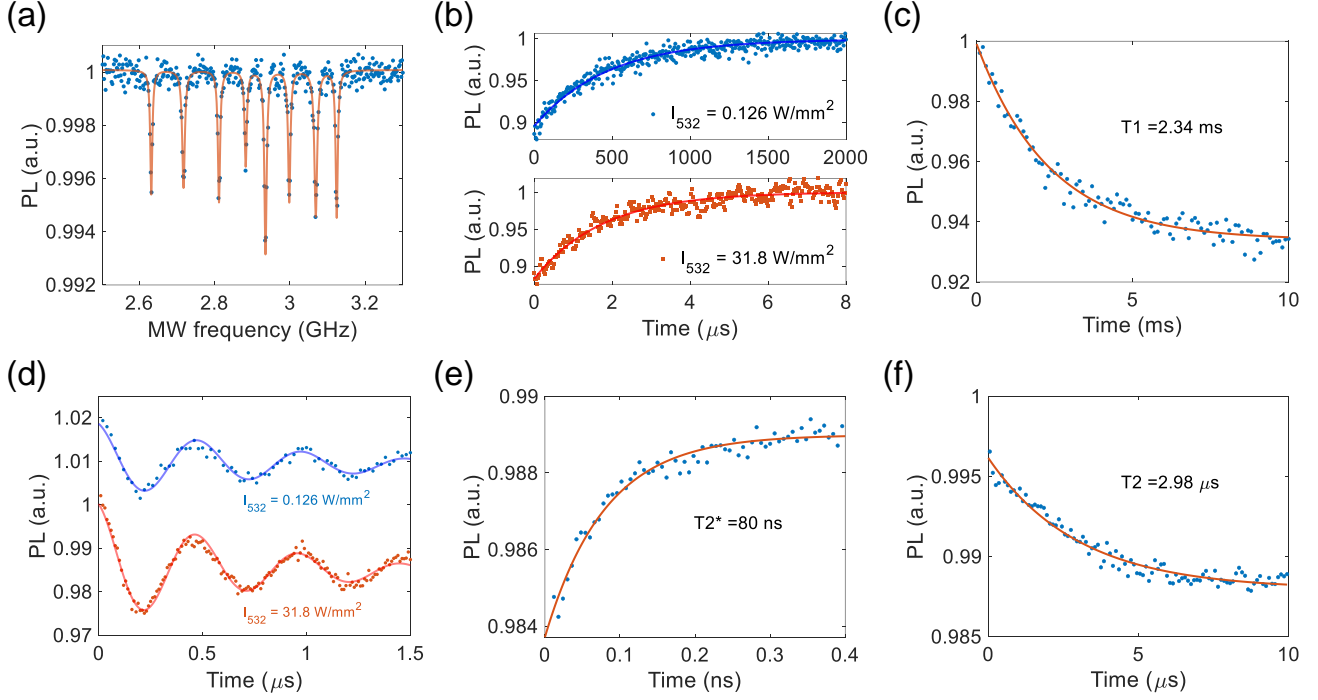
The unit vector of the direction of the magnetic field of microwave is $\mathbf{n}_{MW} = (0, -\sin \theta', \cos \theta')$. So the angle between the NV spin and the microwave is $\arccos(\cos \theta \cos \theta' - \sin \phi(t) \sin \theta \sin \theta')$. The effective magnetic field of microwave is

$$B_{MW}^\perp = B_{MW} \sqrt{1 - (\cos \theta \cos \theta' - \sin \phi(t) \sin \theta \sin \theta')^2}. \quad (\text{E3})$$

Rabi frequency is proportional to the effective magnetic field of microwave, $\Omega_{Rabi} \propto B_{MW}^\perp$. Therefore, it is necessary to synchronize the measurement cycle and the rotation signal of the levitated nanodiamond, and apply microwave pulse at the same rotation phase in repeated Rabi oscillation measurements.

Appendix F: Nanodiamond fixed on glass

To compare with a levitated nanodiamond, we carry out the quantum measurement of a nanodiamond fixed on a glass cover slip, with a thickness of $300 \mu\text{m}$. The glass cover slip is placed at the center of the surface ion trap



Supplemental Fig. 8. Quantum measurement of NV centers in a nanodiamond fixed on a glass. (a) ODMR of the fixed NV centers. (b) Initialization of the nanodiamond Nv centers when the 532 nm laser intensity is 0.126 W/mm^2 (blue circles) or 31.8 W/mm^2 (red squares). The initialization times are 0.469 ms and $1.77 \mu\text{s}$, respectively. (c) Experimental T_1 measurement of the nanodiamond. The T_1 is 2.34 ms . (d) Rabi oscillations of the nanodiamond when the 532 nm laser intensity is 0.126 W/mm^2 (blue circles) or 31.8 W/mm^2 (red squares). The Rabi frequencies are both 1.99 MHz and the decay times T_2^{rabi} are $0.845 \mu\text{s}$ and $0.904 \mu\text{s}$, respectively. (e) Experimental Ramsey measurement. The T_2^* of the nanodiamond NV centers fixed on a glass is 80 ns . (f) Spin Echo measurement, which indicates a T_2 of $2.98 \mu\text{s}$.

to keep the direction and power of microwave unchanged compared to a levitated nanodiamond. Supplementary Fig. 8(a) is the ODMR of the nanodiamond. The linewidth is smaller than that of a levitated nanodiamond. The initialization time are measured at $I_{532} = 0.126 \text{ W/mm}^2$ (blue circles) and $I_{532} = 31.8 \text{ W/mm}^2$ (red squares in Supplementary Fig. 8(b)) for comparison. The initialization times are 0.469 ms and $1.77 \mu\text{s}$, respectively. T_1 of the nanodiamond on glass surface is 2.34 ms (Supplementary Fig. 8(c)), which is close to that of a levitated one. We measure Rabi oscillation at weak 532 nm laser ($I_{532} = 0.126 \text{ W/mm}^2$), which is similar to the intensity used for a levitated nanodiamond in high vacuum (Supplementary Fig. 8(d)). We get the similar result with high intensity of 532 nm laser ($I_{532} = 31.8 \text{ W/mm}^2$). The Rabi frequency is 1.99 MHz and the decay time T_2^{Rabi} are $0.845 \mu\text{s}$ and $0.904 \mu\text{s}$, respectively. Supplementary Fig. 8(e) shows the Ramsey measurement, while Supplementary Fig. 8(f) is the spin echo measurement. The corresponding values for T_2^* and T_2 are 80 ns and $2.98 \mu\text{s}$, respectively.